Monthly Notices of the ROYAL ASTRONOMICAL SOCIETY

MNRAS **527,** 8511–8534 (2024) https://doi.org/10.1093/mnras/stad3722
Advance Access publication 2023 December 01

The FLASH pilot survey: an H I absorption search against MRC 1-Jy radio sources

J. N. H. S. Aditya [1,2]★ Hyein Yoon,[1,2] James R. Allison [2,3] Tao An [4,5] Rajan Chhetri [6,7] Stephen J. Curran,[8] Jeremy Darling,[9] Kimberly L. Emig,[10] Marcin Glowacki [11] Emily Kerrison [1,2,12] Bärbel S. Koribalski [12,13] Elizabeth K. Mahony [12] Vanessa A. Moss,[12] John Morgan,[7] Elaine M. Sadler [1,2,12] Roberto Soria [1,14,15] Renzhi Su,[4,5,12] Simon Weng [1,2] and Matthew Whiting[12]

[1]*Sydney Institute for Astronomy, School of Physics A28, University of Sydney, NSW 2006, Australia*
[2]*ARC Centre of Excellence for All Sky Astrophysics in 3 Dimensions (ASTRO 3D), Sydney, Australia*
[3]*First Light Fusion Ltd, Unit 9/10 Oxford Pioneer Park, Mead Road, Yarnton, Kidlington OX5 1QU, UK*
[4]*Shanghai Astronomical Observatory, 80 Nandan Road, Shanghai 200030, China*
[5]*School of Astronomy and Space Sciences, University of Chinese Academy of Sciences, 19A Yuquan Road, Beijing 100049, China*
[6]*ATNF, CSIRO Space and Astronomy, P.O. Box 1130, Bentley, WA 6102, Australia*
[7]*International Centre for Radio Astronomy Research, Curtin University, GPO Box U1987, Perth, WA 6845, Australia*
[8]*School of Chemical and Physical Sciences, Victoria University of Wellington, PO Box 600, Wellington 6140, New Zealand*
[9]*Center for Astrophysics and Space Astronomy, Department of Astrophysical and Planetary Sciences, University of Colorado, 389 UCB, Boulder, CO 80309-0389, USA*
[10]*National Radio Astronomy Observatory, 520 Edgemont Road, Charlottesville, VA 22903, USA*
[11]*International Centre for Radio Astronomy Research (ICRAR), Curtin University, Bentley, WA 6102, Australia*
[12]*ATNF, CSIRO Space and Astronomy, PO Box 76, Epping, NSW 1710, Australia*
[13]*School of Science, Western Sydney University, Locked Bag 1797, Penrith, NSW 2751, Australia*
[14]*INAF – Osservatorio Astrofisico di Torino, Strada Osservatorio 20, I-10025 Pino Torinese, Italy*
[15]*College of Astronomy and Space Sciences, University of the Chinese Academy of Sciences, Beijing 100049, China*

Accepted 2023 November 29. Received 2023 November 29; in original form 2023 October 6

ABSTRACT

We report an ASKAP search for associated H I 21-cm absorption against bright radio sources from the Molonglo Reference Catalogue (MRC) 1-Jy sample. The search uses pilot survey data from the ASKAP First Large Absorption Survey in H I (FLASH) covering the redshift range $0.42 < z < 1.00$. From a sample of 62 MRC 1-Jy radio galaxies and quasars, we report three new detections of associated H I 21-cm absorption, yielding an overall detection fraction of 1.8 per cent$^{+4.0\ \mathrm{per\ cent}}_{-1.5\ \mathrm{per\ cent}}$. The detected systems comprise two radio galaxies (MRC 2216−281 at $z = 0.657$ and MRC 0531−237 at $z = 0.851$) and one quasar (MRC 2156−245 at $z = 0.862$). The MRC 0531−237 absorption system is the strongest found to date, with a velocity integrated optical depth of 143.8 ± 0.4 km s^{-1}. All three objects with detected H I 21-cm absorption are peaked-spectrum or compact steep-spectrum (CSS) radio sources. Two of them show strong interplanetary scintillation at 162 MHz, implying that the radio continuum source is smaller than 1 arcsec in size even at low frequencies. Among the class of peaked-spectrum and compact steep-spectrum radio sources, the H I detection fraction is 23 per cent$^{+22\ \mathrm{per\ cent}}_{-13\ \mathrm{per\ cent}}$. All three detections have a high 1.4 GHz radio luminosity, with MRC 0531−237 and MRC 2216−281 having the highest values in the sample, > 27.5 W Hz^{-1}. The preponderance of extended radio sources in our sample could partially explain the overall low detection fraction, while the effects of a redshift evolution in gas properties and AGN UV luminosity on the neutral gas absorption still need to be investigated.

Key words: galaxies active – galaxies high redshift – quasars absorption lines – radio lines galaxies.

1 INTRODUCTION

Neutral hydrogen (H I) is the most abundant gaseous element in the interstellar medium of galaxies, and acts as a key reservoir for star formation, particularly in its cold phase (e.g. Krumholz, McKee & Tumlinson 2009). Probing the distribution of H I is hence critical for understanding the evolution of galaxies. H I can be traced using the Lyman α ($n = 2$-1 transition; Ly α) and the hyperfine H I 21-cm transitions in the hydrogen atom. The Ly α transition traces both the cold and warm phases of the neutral gas, however, in general the line is not a good indicator of gas kinematics because of the complex radiative transfer mechanism involved (see e.g. Cantalupo et al. 2005). Most observations of this line are conducted for high redshift ($z > 1.7$) galaxies, as the rest-frame wavelength of the transition, 1215.6 Å, redshifts to the optical bands, which in turn can be observed using ground based optical telescopes (Noterdaeme et al. 2012; Bird, Garnett & Ho 2017). The H I 21-cm hyperfine transition is an

★ E-mail: adi.jnhs@gmail.com, aditya.jammalamadaka@sydney.edu.au

excellent alternative to trace neutral gas in galaxies from low-to-high redshifts (Kanekar & Briggs 2004), and the neutral gas can be detected through both H I 21-cm emission and absorption. In the case of H I 21-cm emission, the signal strength is solely dependent on the H I column density, and, given the sensitivity limitations of the currently available telescopes, the H I 21-cm emission from individual galaxies has been detected in systems up to a redshift of only $z \approx 0.376$ (Fernández et al. 2016). An exception to this is a recent detection at $z \approx 1.3$, where the emission is strongly boosted by a gravitational lens (Chakraborty & Roy 2023). On the other hand, H I can also be detected in absorption arising against a background radio source which could be powered by an active galactic nucleus (AGN). Here, the signal strength is dependent on both the H I column density and the strength of the background radio source, and hence, against bright radio sources the absorption strength is independent of redshift.

1.1 Associated H I absorption in radio AGN

'Associated' H I 21-cm absorption defined to be within 3000 km s^{-1} of the AGN redshift (see e.g. Gupta et al. 2021) is thought to arise from within the AGN host galaxy, whereas for intervening absorbers the gas is located somewhere along the line of sight towards a background source. The observed absorption line will be a summation of the features arising from individual clouds that intercept our line of sight towards the radio source, and the combined signal strength is sensitive to the cold component of the gas (see e.g. Kanekar & Briggs 2004).

In the case of associated systems, the absorption profile can be used to understand the overall motion of the gas relative to the AGN. Absorption that is redshifted with respect to the AGN systemic redshift could indicate gas inflows, whereas blueshifted features could indicate outflowing gas pushed out either by starbursts or the expanding AGN jets (e.g. Vermeulen et al. 2003; Morganti et al. 2013; Maccagni et al. 2017). However, we note that such features could also represent gas clouds (particularly in the narrow-line regions) or disc-like structures rotating around the nucleus. The shape and the width of the absorption can be used to infer the structure and location of the absorbing gas in some cases. For example, features with either narrow (full width at half-maximum, FWHM $\lesssim$ few $\times$ 100 km s^{-1}) and deep absorption, and/or with a double-horned profile would indicate that the gas could be located in a disc-like rotating structure around the nucleus (see e.g. Murthy et al. 2021). Whereas, wide and shallow profiles, with signatures of disturbed kinematic features would indicate jet–gas interactions that could be perturbing the surrounding gas (Morganti et al. 2013; Aditya & Kanekar 2018a). The key advantages of the associated H I 21-cm absorption studies are namely, the strength of absorption (arising from an isolated cloud against a background radio source) being independent of redshift, absorption being a good tracer of cold gas that is believed to be the precursor for star formation, and the line being sensitive to the gas kinematics. These advantages make these studies suitable for understanding the physical conditions of neutral gas in the host galaxies of AGN at various redshifts.

1.2 Targeted searches for associated H I 21-cm absorption

Over a thousand radio sources have been targeted in searches for associated H I 21-cm absorption at redshifts $0.1 < z < 5$ (e.g. Pihlström, Conway & Vermeulen 2003; Vermeulen et al. 2003; Gupta et al. 2006; Carilli et al. 2007; Curran & Whiting 2010; Allison et al. 2015; Curran et al. 2016a; Maccagni et al. 2017; Aditya & Kanekar 2018b; Grasha et al. 2019; Murthy et al. 2022).

Most of the detections ($\approx$190) made in these searches are associated with low-redshift ($z \lesssim 0.4$) systems, and only eleven detections have been reported at $z > 1$ (see Chowdhury, Kanekar & Chengalur 2020, and references therein). The detection fraction in systems at $z \gtrsim 1$ was found to be significantly lower ($\approx 3\sigma$) in the combined sample of all literature searches for associated H I 21-cm absorption (Curran et al. 2019). The H I 21-cm absorption strength was also found to be significantly lower ($\approx 3.5\sigma$) at $z > 1$ in a sample of compact flat-spectrum radio sources studied by Aditya & Kanekar (2018b). Grasha et al. (2019) deduced similar results in their sample of 89 compact radio sources distributed over redshifts $0 < z < 3.8$.

The main explanation for the low detection fraction is that the relatively higher ultraviolet (UV) luminosities of the high-redshift optically selected AGNs would ionize the surrounding neutral gas, thereby reducing the H I optical depth (Curran et al. 2008, 2019). However, it has long been known that the proximity of neutral gas to a strong radio source could alter the hyperfine populations, and raise the spin temperature of the gas (Field 1959), and as well reduce the optical depth of the gas. And so, the higher radio luminosities of the optically selected high-z AGNs could be an alternative explanation for the lower detection rate at high redshifts (e.g. Aditya & Kanekar 2018b). Further, Kanekar et al. (2014) found that the absorption-selected damped Ly α systems at high redshifts typically have higher spin temperatures, probably due to inefficient cooling therein, which could as well be the case in AGN host galaxies (i.e. for 'associated' H I absorption systems) (see e.g. Aditya & Kanekar 2018b; Murthy et al. 2022). Despite the efforts of various studies mentioned above, it is not yet clear to what level of significance the above factors affect the H I 21-cm absorption strength at high redshifts, and, if any of these factors is dominant compared to others.

We note that nearly all earlier studies used targeted searches where the samples were selected based on specific radio spectral or optical properties.

The number density of the searches is unevenly distributed across redshift intervals, with the intermediate redshifts $0.4 < z < 1.0$ having only $\approx$ 15 per cent of the total (see Curran et al. 2019) and being dominated by compact radio sources (see e.g. Grasha et al. 2019). Such differences in the samples across redshift could introduce biases in the interpretations. Indeed, it is already known that the detection fraction in compact radio sources is relatively high compared to extended sources, due to a high gas covering factor in compact sources (Gupta et al. 2006; Curran et al. 2013c; Maccagni et al. 2017). Thus an unbiased estimate of the detection fraction and the overall absorption strength at intermediate redshifts is currently not available. Although the study of a small sample of 11 targets (at $0.7 < z < 1.0$) analysed by Aditya (2019) resulted in four new detections, indicating that the detection fraction could be as high as 30 per cent, similar to that at low redshifts, larger samples of 89 and 24 sources studied by Grasha et al. (2019) and Murthy et al. (2022), respectively, yielded no new detections at these redshifts. It should, however, be pointed out that while the sample size of Aditya (2019) is quite small to obtain reliable statistics, the samples chosen by Grasha et al. (2019) and Murthy et al. (2022) consist of strictly compact and extended radio sources, respectively. The observed trend of decreasing detection rate of the H I 21-cm absorption line at higher redshifts, if confirmed, has significant implications for our understanding of galactic evolution and its gaseous components. The causes for this trend are not yet clear; the biases in previous studies due to restricted range of source luminosities and redshifts, need to be addressed. Therefore, further studies should be conducted by including a more diverse and balanced sample distribution across different redshifts and radio source types.

1.3 This paper

The First Large Absorption Survey in H I (FLASH; Allison et al. 2022) is a large-area survey to search for H I 21-cm absorption at intermediate redshifts, $0.42 < z < 1.00$ (covering a frequency range of ∼700–1000 MHz), using the ASKAP radio telescope (Hotan et al. 2021). The survey is planned to cover almost the entire southern sky (excluding $|b| < 8.5$ deg) and two pilot surveys have recently been completed. While the pilot surveys have covered a total of ∼3000 deg^2 of the sky, the full survey will span ∼25 000 deg^2 (see Yoon et al., in preparation). We note that the sources in the survey have no prior selection criterion. In this paper we report the results of FLASH observations towards a sample of bright radio sources from the Molonglo Radio Catalogue 1 Jy (MRC 1-Jy; McCarthy et al. 1996; Kapahi et al. 1998a, b).

In the below sections, we describe the properties of the MRC sample, FLASH pilot observations towards the MRC sources and data reduction, the radio properties of the MRC sample used in this paper, the new detections of H I 21-cm from our observations, and finally the deductions from our results. We adopt a ΛCDM cosmology with $H_0 = 70$ km s^{-1} Mpc^{-1}, $\Omega_m = 0.3$, and $\Omega_\Lambda = 0.7$ for our estimates.

2 THE MOLONGLO REFERENCE CATALOGUE AND THE MRC 1-JY SAMPLE

The Molonglo Reference Catalogue (MRC; Large et al. 1981) is a catalogue of over 12 000 radio sources with a flux density above 0.7 Jy at 408 MHz, derived from a survey of 7.85 sr of sky carried out by the Molonglo Radio Telescope between 1968 and 1978. The catalogue is substantially complete above a 408 MHz flux density of 1.0 Jy. Large et al. (1981) note that the reliability of the catalogue, in terms of completeness, is >99.9 per cent.

The MRC 1-Jy sample (McCarthy et al. 1996; Kapahi et al. 1998a, b) is a complete sample of 560 radio sources with $S_{408\ \mathrm{MHz}} \rangle 0.95$ Jy within a 0.59 sr region of sky defined as follows:

RA (B1950)	between 09h20m and 14h04m, or between 20h20m and 06h14m;
Dec (B1950)	between −20° and −30°

The MRC 1-Jy sample is relatively unbiased, in the sense that only the radio flux density was used to select the sample members. The sample contains a mixture of radio galaxies (McCarthy et al. 1996) and quasars (Kapahi et al. 1998a; Baker et al. 1999).

Detailed information about the radio structure on arcsec scales, obtained through VLA observations at either 4.8 GHz (*C* band) or 1.4 GHz (*L* band), is available for most of the MRC 1-Jy sources. Optical and or infrared identifications, astrometry, and *r*-band magnitudes are also available for a large fraction of the sample (Kapahi et al. 1998b).

Importantly, 393 sources (≈ 70 per cent) of the MRC 1-Jy sample have spectroscopic redshifts available either from the optical follow-up observations by the authors, or from later studies in the literature (e.g. Pocock et al. 1984; McCarthy et al. 1996; Kapahi et al. 1998a, b; Brown, Webster & Boyle 2001). Among the 393 sources with redshifts, 217 have $0.4 < z < 1.0$; these 217 high redshift sources are suitable for searches for H I 21-cm absorption in the FLASH survey (see Section 3.1). The remaining 167 sources in the MRC 1-Jy catalogue do not have spectroscopic redshifts available presently. The main reason for non-availability of redshifts is that most targets among these are not covered in existing optical spectroscopic surveys like SDSS.

The three main characteristics of the sample, namely, the unbiased selection of radio sources, the flux densities being $\gtrsim 1$ Jy at low radio frequencies, and the availability of optical redshifts for a large fraction of the sample, makes it highly suitable for H I 21-cm absorption studies. The high radio flux densities allow us to achieve stringent optical depth sensitivity in a reasonable integration time, while the optical redshifts allow us to assess whether an H I absorber is associated with the source, and if so, to assess the kinematics of the gas relative to the AGN.

For this reason, the fields observed in the two FLASH pilot surveys (Yoon, H. et al., in preparation) were selected to cover a substantial fraction of the MRC 1-Jy survey area.

3 FLASH PILOT SURVEY OBSERVATIONS IN THE MRC 1-JY REGION

3.1 FLASH pilot surveys

The ASKAP radio interferometer is located at Inyarrimanha Ilgari Bundara, CSIRO's Murchison Radio-Astronomy Observatory, and consists of 36 antennas, each 12 m in diameter, with a maximum baseline of 6 km (DeBoer et al. 2009; Hotan et al. 2021). The observing frequency range is 0.7–1.8 GHz, and has an instantaneous bandwidth of 288 MHz that can be split into 18.5 kHz channels. These features are suitable for the studies of H I 21-cm absorbers from the local Universe out to redshift $z \approx 1.0$.

Based on the ASKAP sensitivity characteristics, a frequency range of 711.5 to 999.5 MHz was chosen for the FLASH survey in order to optimize the discovery potential and detection yield of H I 21-cm absorption systems (Allison et al. 2022). For a system at redshift $z \approx 1$, the 18.5 kHz channel width corresponds to a velocity width of ≈ 7.6 km s^{-1}. This is sufficient to resolve the typical narrow absorption lines of few × 10 km s^{-1}, discovered in the literature (Maccagni et al. 2017).

A total observing time of 200 h was allocated to the two pilot surveys of FLASH. The observations for the first pilot survey were conducted from 2019 December to 2020 September. Each ASKAP field, with a size of 6.4 × 6.4 deg^2, was observed for two hours, and the typical noise characteristics are described in Table 1. Eleven fields of this survey have a complete overlap, and one field has a partial overlap, with the regions of sky covered by the MRC 1-Jy sample. For the MRC fields, the median RMS noise on the continuum is 92 μ Jy beam^{-1}, and for the spectra the median is 4.65 mJy beam^{-1} per 18.5 kHz channel, measured in the central part of the frequency band. This is consistent with an estimated range of 3.2–5.1 mJy beam^{-1} ch^{-1}, noted in table 1 of Allison et al. (2022). The median continuum RMS noise for both pilot 1 and 2 observations is 92 μJy beam^{-1}, and, the median spectral RMS noise is 4.81 and 4.65 mJy beam^{-1} ch^{-1}, respectively.

The second pilot survey was carried out from 2021 November to 2022 August. Seven fields have a complete overlap and six fields have partial overlap with the MRC 1-Jy region of sky. Among the above, one field was also observed in the first pilot survey. A few of the fields were repeated in both first and second surveys for multiple reasons; to test the data quality, to re-observe specific fields where data were corrupted, and to confirm any tentative detection. Standard observing techniques as described by Hotan et al. (2021) and McConnell et al. (2020) were used in both of the pilot surveys. The bright radio source PKS B1934-638 was used for primary calibration, and also to set the flux density scale.

Table 1. Summary of observations of the 23 FLASH Pilot Survey fields overlapping with the MRC 1-Jy survey area. The columns are: (1) the field name, (2) the unique CASDA scheduling block identification (SBID) assigned to each observation, (3) and (4) the RA and DEC of the pointing centres, (5) the date of observation, (6) the width of beam-forming interval used in the observations, (7) the RMS noise on the continuum, for region within 3.2 deg of the phase centre, (8) the spectral root mean square (RMS) noise per 18.5 kHz channel in the central part of the frequency band, and for the sources within 3.2 deg of the phase centre, (9) and (10) the sizes of the synthesized beams in continuum and spectral cubes. SBIDs in the range 10 849 to 15 212 were observed during the first FLASH Pilot Survey, while those from 34 547 to 37 797 were observed during the second pilot survey. The observing time for the below mentioned SBIDs was 2 h each.

Name	CASDA SBID	Pointing centre RA [J2000]	Pointing centre Dec. [J2000]	Obs. date UTC	BF (MHz)	$\sigma_{\rm cont}$ (μJy beam^{-1})	$\sigma_{\rm line}$ (mJy beam^{-1} channel^{-1})	Synthesized beam (arcsec) Continuum	Synthesized beam (arcsec) Line
(1)	(2)	(3)	(4)	(5)	(6)	(7)	[8]	[9]	[10]
FLASH_302P	10 850	00:00:00.15	−25:07:52.2	17-12-2019	5	102	5.03	20.0 × 14.6	30.4 × 28.6
FLASH_303P	11 053	00:27:10.19	−25:07:47.2	05-01-2020	5	123	4.83	19.7 × 14.3	29.9 × 26.9
FLASH_304P	13 291	00:54:20.38	−25:07:47.2	19-04-2020	9	93	4.62	18.3 × 11.2	30.9 × 22.7
FLASH_305P	13 372	01:21:30.50	−25:07:47.2	22-04-2020	9	90	4.84	16.9 × 11.0	30.3 × 22.7
FLASH_305P	37 449	01:21:30.57	−25:07:47.2	18-02-2021	5	90	4.65	15.1 × 13.2	24.5 × 21.8
FLASH_306P	37 475	01:48:40.70	−25:07:47.2	19-02-2022	5	116	4.65	21.4 × 12.1	31.7 × 18.8
FLASH_306P	13 281	01:48:40.75	−25:07:47.2	18-04-2020	9	84	4.51	13.7 × 11.4	27.0 × 22.9
FLASH_255P	35 939	01:52:56.47	−31:23:14.7	15-01-2021	5	81	4.40	12.7 × 11.9	22.2 × 20.1
FLASH_255P	41 226	01:52:56.63	−31:23:20.8	03-06-2022	2	85	4.65	14.5 × 11.3	24.6 × 19.6
FLASH_307P	13 268	02:15:50.94	−25:07:47.2	17-04-2020	9	85	4.56	14.6 × 11.3	27.9 × 22.8
FLASH_308P	15 212	02:43:01.13	−25:07:47.2	04-07-2020	9	91	4.57	13.0 × 11.8	22.8 × 20.1
FLASH_257P	37 451	02:49:24.70	−31:23:14.7	18-02-2022	5	87	4.84	17.4 × 12.4	27.4 × 21.2
FLASH_309P	13 269	03:10:11.32	−25:07:47.2	17-04-2020	9	93	4.56	18.6 × 11.0	31.2 × 22.7
FLASH_258P	37 452	03:17:38.82	−31:23:14.7	18-02-2021	5	79	4.58	13.8 × 11.6	22.5 × 19.4
FLASH_310P	37 432	03:37:21.51	−25:07:47.2	17-02-2021	5	110	4.75	21.8 × 11.5	32.7 × 18.7
FLASH_312P	37 797	04:31:41.89	−25:07:47.2	02-03-2022	5	107	5.13	22.6 × 11.5	33.4 × 18.7
FLASH_313P	34 547	04:58:52.08	−25:07:47.2	17-12-2021	5	107	4.60	19.2 × 11.6	30.6 × 19.3
FLASH_314P	34 570	05:26:02.26	−25:07:47.2	19-12-2021	5	104	4.52	18.2 × 11.6	29.3 × 19.3
FLASH_314P	41 061	05:26:02.41	−25:07:52.2	29-05-2022	5	78	4.53	13.5 × 11.9	22.3 × 20.5
FLASH_377P	34 571	09:36:00.00	−18:51:45.4	19-12-2021	5	92	4.81	13.1 × 12.1	22.7 × 20.0
FLASH_378P	34 561	10:02:10.90	−18:51:45.4	18-12-2021	5	101	4.79	22.2 × 11.8	34.3 × 19.1
FLASH_351P	10 849	22:11:19.25	−25:07:47.2	17-12-2019	5	101	4.80	19.7 × 14.3	30.1 × 28.0
FLASH_352P	11 051	22:38:29.43	−25:07:47.2	05-01-2020	5	92	5.07	16.2 × 11.7	25.2 × 22.8
FLASH_353P	11 052	23:05:39.62	−25:07:47.2	05-01-2020	5	92	4.98	17.9 × 12.2	27.0 × 23.4
FLASH_354P	13 279	23:32:49.81	−25:07:47.2	18-04-2020	9	87	4.90	13.2 × 11.6	26.4 × 22.4

3.2 Data reduction

The standard data reduction pipeline for ASKAP, described in Whiting (2020) and Hotan et al. (2021) was used for initial data processing. The data reduction steps include calibration, continuum imaging, spectral cube imaging, continuum subtraction, production of continuum source catalogues, spectra extraction, and measurement of a range of quality control parameters. The median RMS noise achieved on the continuum for the pilot survey fields, for a region within 3.2 deg of the phase centre is 93μ Jy beam^{-1}. And, the median RMS noise per 18.5 kHz channel in the central part of the frequency band, and for the source within 3.2 deg of the phase centre is 4.75 mJy beam^{-1}. The median resolution of the synthesized beam on the continuum images is 18.2 arcsec × 11.7 arcsec. The synthesized beam sizes for the fields can be seen in Table 1. A complete description of these aspects and the data-reduction steps, specific to FLASH survey, will be given in our forthcoming data release paper (Yoon et al., in preparation).

The reduced pipeline (ASKAPsoft) data products for the pilot surveys 1 and 2 were released through the CSIRO ASKAP Science Data Archive (CASDA) https://research.csiro.au/casda/. The data products include continuum catalogues, continuum images and cubes, spectral-line cubes, individual spectra at the location of the continuum sources, and validation reports.

The pipeline does two rounds of continuum subtraction; first in the visibility domain by subtracting the components from the self-calibrated data, and then, an image-based continuum subtraction to clean up any residual continuum. The spectral-line data of pilot 1 observations, released through CASDA, were processed using 1 MHz intervals while smoothing the bandpass solutions, and during continuum subtraction using the spectral cube. Due to this, broad absorption lines with widths larger than $\approx$ 300 km s^{-1} were subtracted out during processing, and were not detected in the final spectra (that are available in CASDA). To overcome this issue, a few post-processing steps were carried out by the FLASH team. Here, we undid the image-based continuum subtraction (as this used 1 MHz intervals), and did a second-round of continuum subtraction by fitting a second-order polynomial to the spectra, over 5 or 9 MHz intervals. We note that a method of subtracting the residual continuum features on the scale of the beam-forming frequency intervals, was developed for ASKAP commissioning work by Allison et al. (2015, 2017). Further details on these procedures, and details on the beam-forming frequency intervals, will be described in detail in Yoon, H. et al. (in preparation). In this paper we use these 'post-processed' spectra for our analysis, and these results will also be released through CASDA in future, as part of a 'value-added' FLASH data release. For pilot 2 observations the image-based continuum subtraction was done over a 5 MHz beam-forming intervals, by the ASKAPsoft pipeline. Thus post-processing was not required.

3.3 FLASH observations of MRC 1-Jy sources

We cross-matched the sky coordinates of the radio sources in the MRC 1-Jy catalogue with the source components from the FLASH

pilot survey data catalogues using a search radius of ≈45 arcsec. The beam size in the MRC observations is ≈2 arcmin (see Kapahi et al. 1998a). We used the TOPCAT (Taylor 2005) software for cross-matching the source coordinates. Out of the 217 sources in the MRC catalogue with redshifts in the range $0.4 < z < 1.0$ (please see Section 2), a total of 64 have counterparts in our pilot survey.

The redshifted H I 21-cm line for the targets MRC 0337–216 and MRC 0055–258 ($z = 0.414$ for both) falls at the edge of the ASKAP band, so we removed these two sources from our sample. Further, for the sources MRC 0930–200, MRC 1002–215, and MRC 1002–216 the band is corrupted by ripples in the band; we conservatively use a peak-to-peak value on the spectrum, instead of the RMS, for estimating the upper limits on the H I integrated optical depths. The source MRC 0201–214 lies at the edge of the FLASH beam, and a part of the continuum was chopped-out in the image. However, the peak of the continuum lies within the beam and we could extract the spectrum at the location. Our final sample has 62 targets, which are the main focus of this paper.

Our sample includes 40 galaxies and 22 quasars. The quasar fraction of 35 per cent is higher than in the full MRC-1Jy catalogue (20 per cent quasars). This reflects the higher redshift completeness of the MRC-1Jy sample for objects with strong optical emission lines. We note that McCarthy et al. (1996) quote a spectroscopic completeness of ∼60 per cent for galaxies, while the completeness for quasars is ∼100 per cent in the MRC sample.

In Fig. 1, we show examples of ASKAP continuum images, FLASH H I 21-cm spectra covering ∼ 3000 km s^{-1} on each side of the AGN redshift (except for those which fall at the edge of ASKAP band), and the radio SEDs. The data for the remaining targets are provided in the online version of the paper, details of which can be seen here.[1] In Table Table 2 we list three new H I 21-cm absorbers detected in our sample. In Table 3 we list the properties of continuum emission and spectra of compact sources that have a single continuum component, with peak flux density >40 mJy, while Table 4 lists details of sources with multiple components that have peak flux density >40 mJy.

4 RADIO PROPERTIES OF THE MRC 1-JY SAMPLE

4.1 ASKAP and VLA-5GHz radio sizes

In our sample of 62 radio sources, 25 are single-component sources in our ASKAP continuum images, while the remaining 37 sources are best fitted by multiple components (see Tables 3 and 4, respectively). The typical resolution in our ASKAP images is ≈15 arcsec at 856 MHz, which is insufficient to ascertain the radio morphology on kiloparsec scales. As a result, the single-component sources in Table 3 could still have an extended morphology on scales of a few kpc to tens of kpc. For these single-component sources, we used the 5-GHz radio images published by Kapahi et al. (1998a, b) to classify the sources as either compact or extended (lobe-dominated, core + lobes, core + hotspots, and hotspot with no core). On this basis, 14 of the single-component sources are core-dominated at 5 GHz and classified as compact in Table 3, while the remaining 48 have extended morphology. We note that in the SUMSS radio survey (Mauch et al. 2003) conducted at 843 MHz, among the sources with flux densities $S_{843\mathrm{MHz}} > 50$ mJy, the number density of steep-spectrum radio sources (with $\alpha^{843}_{1400} < -0.5$) is at least three times larger than the flat-spectrum radio sources ($|\alpha^{843}_{1400}| < 0.5$). Compact radio sources tend to have flatter radio spectra compared to extended sources (e.g. Wang et al. 1997; Healey et al. 2007). The SUMSS survey results thus imply a preponderance of extended sources among bright radio sources (S > 50 mJy) surveyed at ∼850 MHz. We can, thus, expect a high fraction of extended radio sources in our 'full' FLASH survey, similar to the number fraction in the current MRC sample.

4.2 Radio SEDs

Further, we used the low radio frequency spectral-energy distribution (SED) as an indicator of compactness of the radio source. For this purpose, we collected the integrated flux densities at frequencies ≈ 70 MHz − 5 GHz of all sources from the literature (Becker, White & Helfand 1995; Douglas et al. 1996; Condon et al. 1998; Kapahi et al. 1998a, b; Mauch et al. 2003; Wayth et al. 2015; Intema et al. 2017), and fit SEDs based on the following models to the data: 1. power-law (PL) and re-triggered (power-law embedded with a peaked-spectrum profile) 2. peaked-spectrum (PS; see equation 1) 3. a high-frequency turnover (HFT)

The SED fitting code is available at https://doi.org/10.5281/zenodo.8336847. A typical radio source with an extended morphology is expected to have a power-law spectrum, with the radio flux density decreasing rapidly with frequency due to synchrotron energy losses. On the other hand, a peaked-spectrum source is expected to be compact, since here, the radio source would be embedded in a dense medium and the radiation would undergo synchrotron self-absorption or free-free absorption, leading to a negative turnover in the spectrum towards low radio frequencies (e.g. O'Dea, Baum & Stanghellini 1991; O'Dea 1998). We use this peaked-spectrum classification to refer collectively to the GPS (gigahertz-peaked spectrum), CSS (compact steep-spectrum), HFP (high-frequency peakers) and MPS (megahertz-peaked spectrum) sources.

A re-triggered model represents the case where the AGN has undergone multiple episodes of nuclear activity (e.g. Callingham et al. 2017). The source would have one or few radio blobs, along with a compact component, yielding a SED which is a combination of a steep-spectrum power-law and a peaked-spectrum component. We note, however, that some of the literature flux density measurements were obtained using instruments with relatively larger observing beams (e.g. the Texas survey at 365 MHz and Molonglo survey at 408 MHz), which could have systematically higher flux estimates. Hence, for the targets for which the significance of the SED curvature could not be assessed, we classified them being consistent with a power-law profile. For targets classified as HFT, the SEDs show a positive turn from a steep power law, at frequencies of few × GHz. These could be cases where a recent flare-up could be happening in the immediate vicinities of the core. Examples of the SED fits are shown in Fig. 1; here we show the plots for six sources, and the full set for the 59 targets (for three targets there are not enough data points available in the literature for obtaining a reliable SED) is available along with the online version of the paper.

Among the 59 SEDs, the fits of 4 sources are consistent with a peaked-spectrum profile, 6 are consistent with HFT, and the remaining 49 are consistent with PL (or steep) profiles. We note that of the four peaked-spectrum sources, three are compact in the 5-

[1]We have included continuum images, H I spectra and the SED fits of all the 62 MRC targets as supplementary material, available with the online version of the paper. The data has a folder with a name 'supplementary_material', which further has three folders with names 'continuum_images', 'sed' and 'spectra'. These folders contain the relevant files of all the sources in this paper.

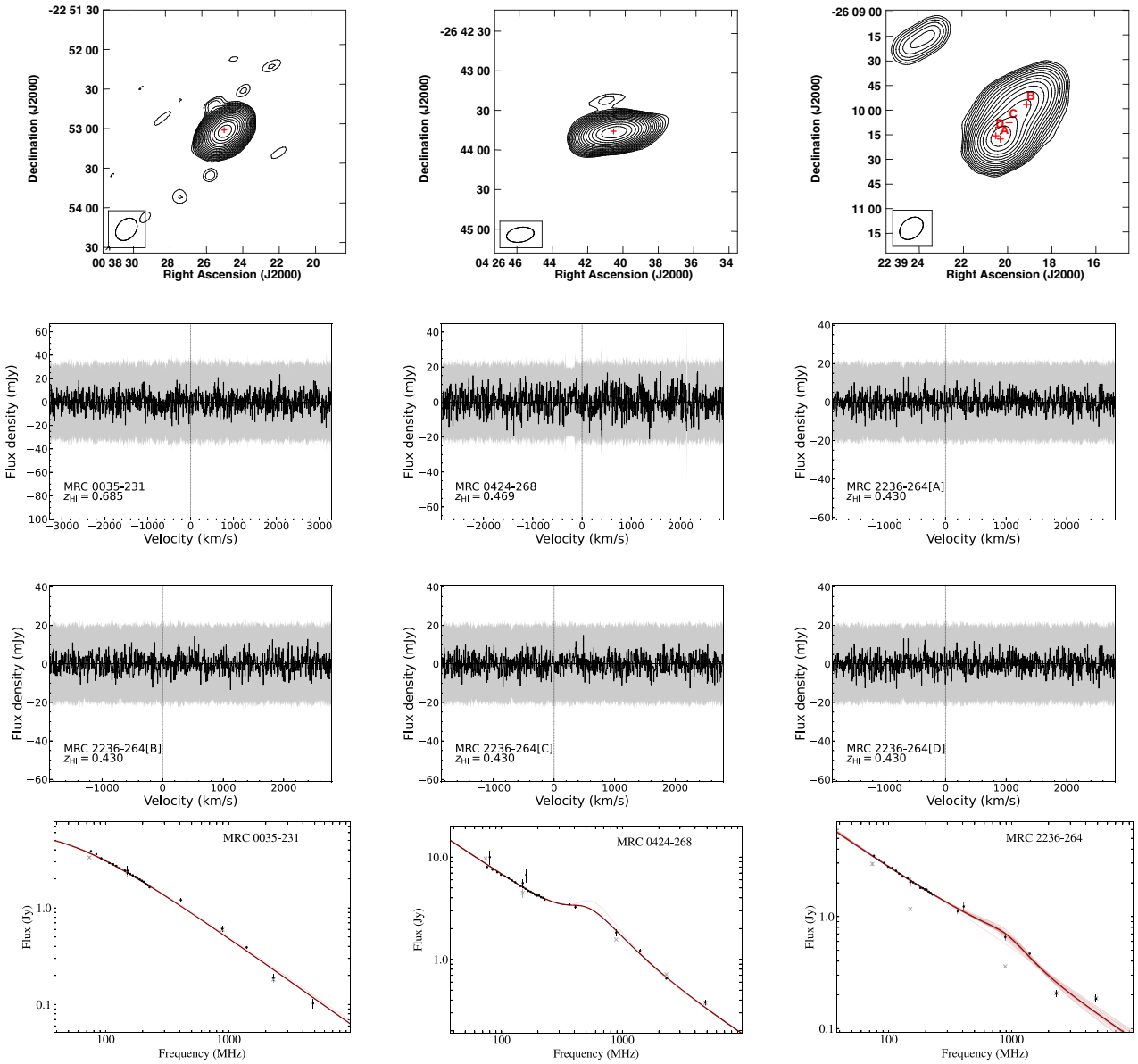

Figure 1. Top row: Examples of ASKAP continuum images of three sources; MRC 0035–231, MRC 0424–268, and MRC 2236–264. The contours are at levels of $5\sigma \times (1, \sqrt{2}, 2, 2\sqrt{2}, 4,$ etc.), where σ is the R.M.S. noise on the continuum image in mJy. MRC 0035–231 and MRC 0424–268 have only a single Gaussian component with peak flux >40 mJy, while MRC 2236–264 has four components with peak flux >40 mJy. The peaks of sources with single components are indicated with a single cross marker. For sources with multiple components the peaks are indicated with cross markers along with alphabetical labels in capitals, matching the corresponding component name in Table 4. Second and third rows: The FLASH pilot spectra for the three sources, extracted at the location of the peak flux density. For MRC 2236–264, four spectra at the locations of the four peaks, with corresponding alphabetical labels are shown. The shaded region corresponds to 3σ R.M.S. noise on the spectrum, and the vertical dashed line corresponds to the AGN redshift. To note: The H I 21-cm line of MRC 2236–264 falls near the edge of ASKAP band. So, velocities at < -2000 km s^{-1} are not shown. Fourth row: The radio SEDs for the three example sources. The fainter lines are iterations of SED fits to the data. And, the faint markers correspond to TGSS (Intema et al. 2017), Texas (Douglas et al. 1996), and Molonglo (Kapahi et al. 1998a, b) surveys, which have relatively larger beams. The same description applies to all continuum images, spectra and other SED fits in this paper, and for the online-only material.

GHz images. And for one of them, MRC 0233–245, while the source is unresolved in 5-GHz maps, two components are detected in the ASKAP image, suggesting that it could have extended structure at low radio frequencies (see also, notes in the Appendix). Further, among the 49 sources with PL profiles, 9 are compact in the 5-GHz images, thus classified as compact steep-spectrum (CSS) sources. We listed the peaked-spectrum and compact steep-spectrum sources from our MRC sample in Table 6.

4.3 Interplanetary scintillation

Interplanetary scintillation (IPS) is the phenomenon in which the flux density of a radio source fluctuates on ∼1-s time-scales due to scintillation induced by turbulent solar wind plasma (Clarke 1964). Only compact sources with sizes <2 arcsec show rapid scintillation, so this technique can hence be used to identify radio sources that have sub-arcsec components without the need to use very large baseline interferometry (e.g. Hewish, Scott & Wills 1964).

Table 2. The parameters of the absorption features in the three detections. The columns are (1) the MRC source name, (2) the source redshift, (3) the peak flux density in ASKAP observations, (4) the integrated flux density, (5) the width of the line at nulls, (6) the peak optical depth, (7) the velocity integrated optical depth, and (8) the H I column density assuming $T_{sp} = 100$ K and a covering factor of unity.

MRC name	z	F_{peak} (mJy)	F_{int} (mJy)	ΔV (km s^{-1})	τ_{peak}	$\int \tau dV$ (km s^{-1})	N_{HI} ($\times 10^{20}$ cm^{-2})
(1)	(2)	(3)	(4)	(5)	(6)	(7)	(8)
MRC 0531–237	0.851	1841.1	1913.6	662.9	0.59	143.80 ± 0.35	262.15 ± 0.64
MRC 2156–245	0.862	805.7	827.7	155.5	0.04	3.12 ± 0.33	5.69 ± 0.60
MRC 2216–281	0.626	3652.8	3706.3	40.7	0.01	0.26 ± 0.04	0.47 ± 0.01

Morgan et al. (2018) have demonstrated that synthesis imaging techniques with the Murchison widefield array (MWA) can be used to detect the IPS signal from a large number of radio sources simultaneously. Observations were made putting the Sun in the null of the primary beam. An image cube with two spatial axes and one time axis, with a time resolution of 0.5s, was constructed to estimate the temporal fluctuation in the source flux densities. A normalized scintillation index (NSI) was calculated from source variability for each source removing the effects of solar elongations (Chhetri et al. 2018).

Radio sources dominated by a sub-arcsec compact component should have a high NSI, ≈1, with angular size comparable to, or smaller than, the Fresnel scale (0.3 arcsec for MWA IPS observations) of the scintillation inducing medium (Little & Hewish 1966).

Fig. 2 shows the expected relationship between source size and NSI at different redshifts. For the redshift range considered in this paper ($0.42 < z < 1$), the normalized scintillation index is expected to be close to 1 for AGN with linear sizes ≲0.5 kpc.

We cross-matched the source coordinates of our sample of 62 targets with an updated catalogue of IPS sources compiled by two of the authors (JM and RC). We found counterparts for 55 of our 62 sources, and the NSI estimates for these sources are listed in Table 5.

For most of our sources, there is good agreement between the angular size at 5 GHz and the NSI values derived at 162 MHz. In particular, all five of the sources with NSI >0.75 (implying source sizes smaller than 2–3 kpc at low frequency) are also unresolved on arcsec scales at 5 GHz. The advantage of the NSI measurements is that they probe structure on smaller scales than the 5 GHz images, and can also reveal the existence of extended low-frequency emission that may not be apparent in high-frequency surveys.

5 FLASH DETECTIONS OF H I 21-CM ABSORPTION

Among the 62 targets, we detected H I 21-cm absorption towards three sources: MRC 0531–237 at $z = 0.851$, MRC 2156–245 at $z = 0.862$, and MRC 2216–281 at $z = 0.626$. The detections were identified initially using an automated line-finding script that uses a Bayesian analysis to identify the absorption lines (Allison et al. 2012), and further confirmed by visual inspection. The parameters of the absorption features are given in Table 2.

Below we describe the characteristics of the radio source, and H I 21-cm absorption in these three targets.

5.1 MRC 0531–237

While detailed optical studies are not available for this source in the literature, McCarthy et al. (1996) reported an optical spectroscopic redshift of $z = 0.851$ (no uncertainty is reported).

The radio source in the ASKAP image at 856 MHz (see left panel of Fig. 3a) is bright with a peak flux density of 1841.1 mJy, and has a dominant core. The milli arcsecond scale VLBI image at 8.4 GHz, archived in the ASTROGEO VLBI data base (see astrogeo), shows an elongated resolved structure extending from north-east to south-west, with a scale of ≈ 465 pc × 97 pc. The north-eastern half of the emission looks relatively diffuse while the south-west half is collimated, though both have similar projected lengths. This suggests probably that the core lies in the central region and the radio lobes are propagating nearly perpendicular to the line of sight. Alternatively, the core could correspond to the south-western node at the end, and the emission could represent a one-sided jet extending to north-east. In both cases, the north-east lobe is likely interacting with a dense ambient medium.

We used the measurements of flux densities at multiple radio frequencies from the literature, to fit a radio SED to the data using the expression:

$$S_\nu = \frac{S_{max}}{1 - e^{-1}} \times \left(\frac{\nu}{\nu_{max}}\right)^{\alpha_{thick}} \times [(1 - e^{-(\frac{\nu}{\nu_{max}})^{\alpha_{thin} - \alpha_{thick}}}], \quad (1)$$

where S_{max}, ν_{max}, α_{thick}, and α_{thin} are peak flux density, peak frequency, optically thick index, and optically thin index, respectively (Snellen et al. 1998). The fit has a clear peaked-spectrum profile (Fig. 3b), with a peak at ≈560.2 MHz, and spectral indices of $\alpha_{thick} = 2.2$ and $\alpha_{thin} = -0.8$. The steep spectrum on the optically thin side is consistent with the extended nature of the radio emission at parsec scales (in the 8.4 GHz VLBI image), and, the turnover of the spectrum at low frequencies, likely due to synchrotron self-absorption or to free–free absorption (e.g. O'Dea, Baum & Stanghellini 1991), indicates that the source is likely embedded in a dense ionized medium.

We detected a strong associated H I 21-cm absorption towards MRC 0531–237, with a peak absorption fraction of 0.35, and a velocity-integrated optical depth of (143.80 ± 0.35) km s^{-1}. The velocity integrated optical depth was estimated using the expression

$$\int \tau(V) dV = -\int \ln\left[1 + \frac{\Delta S}{f * S_c}\right] dV$$

Here, τ is the H I 21-cm optical depth, f is the gas covering factor, which assumed to be unity. This is the strongest known absorber till date, with the highest integrated optical depth; the earlier highest detected value being $\int \tau\, dV = 118.4$ km s^{-1}, towards SDSS J090331+010847 (Su et al. 2022). We estimate a high column density of $(2.62 \pm 0.01) \times 10^{22}$ cm^{-2},

$$N_{HI} = 1.823 \times 10^{18} \times T_s \times \int \tau\, dV$$

(e.g. Morganti & Oosterloo 2018), assuming a spin temperature (T_s) of 100 K. We could fit two Gaussian components to the absorption profile, which is the minimum number with which after subtracting

Table 3. Single-component MRC sources (with peak flux density >40 mJy) observed in our FLASH pilot surveys. The columns are: (1) the source name, (2) the FLASH component ID, (3) the source right ascension, (4) the source declination, (5) the source classification; QSO represents a quasar and G represents a galaxy (6) the source redshift, z, (7) the peak flux density at redshifted H I 21-cm frequency, from our ASKAP observations, (8) the integrated flux density, (9) rms noise on the continuum image in units of mJy per beam, (10) rms noise on the spectrum in mJy per beam per channel, (11) velocity integrated optical depth, $\int \tau dv$, and the 3σ upper limits to optical depth for non-detections, assuming a line width of 100 km s^{-1}, (12) the largest angular size (LAS) of the source, measured at 5 GHz by Kapahi et al. (1998a) for the galaxies and Kapahi et al. (1998b) for the quasars, (13) notes on the radio morphology, based on the 5 GHz images presented by Kapahi et al. (1998a, b).

Source name	Component ID [FLASH]	RA	DEC	Source[1] type	Redshift[2] [z]	F_{peak} (mJy beam^{-1})	F_{int} [mJy]	σ_{image} (mJy beam^{-1})	$\sigma_{channel}$ (mJy beam^{-1})	τ (km s^{-1})	LAS_5 GHz (arcsec)	Notes
(1)	(2)	(3)	(4)	(5)	(6)	(7)	(8)	(9)	(10)	(11)	(12)	(13)
MRC 0030–220	SB11053_component_10a	00:32:44.6	−21:44:21	QSO	0.806	472.5	490.3	0.21	9.5	<2.3	3.9	lobe-dominated
MRC 0035–231	SB11053_component_6a	00:38:24.9	−22:53:03	G	0.685	682.3	711.5	0.20	7.2	<1.1	2.3	compact
MRC 0050–222	SB13291_component_7a	00:52:42.8	−21:55:47	G	0.654	660.6	689.7	0.14	6.7	<0.9	<2	compact
MRC 0106–233	SB13291_component_9a	01:09:02.9	−23:07:30	QSO	0.818	545.4	575.4	0.20	11.6	<1.9	2.5	lobe-dominated
MRC 0118–272	SB37449_component_5a	01:20:31.5	−27:01:23	QSO	>0.557	1220.1	1332.4	0.27	5.4	<0.4	<2	compact, BL Lac
MRC 0144–227	SB13281_component_6a	01:47:09.2	−22:32:41	G	0.600	699.3	720.3	0.11	4.9	<0.6	<2	compact
MRC 0201–214	SB13268_component_15a	02:03:32.1	−21:13:46	G	0.915	421.5	466.5	0.28	26.2	<5.5	<2	compact
MRC 0209–237	SB13268_component_12a	02:11:28.3	−23:28:23	QSO	0.680	403.5	869.4	0.08	4.7	<1.1	18	core + hotspots
MRC 0225–241	SB13268_component_4a	02:27:33.5	−23:54:55	G	0.520	1116.5	1317.4	0.41	5.1	<0.6	5.2	compact triple[a]
MRC 0230–245	SB15212_component_5a	02:32:30.4	−24:22:05	G	0.880	922.4	1284.6	0.57	6.7	<0.8	11.3	lobe-dominated
MRC 0233–290	SB37451_component_1a	02:35:56.2	−28:50:46	G	0.725	922.4	1000.3	0.37	10.6	<1.0	<5	compact
MRC 0319–298	SB37452_component_1a	03:21:28.8	−29:40:45	G	0.583	2858.3	2990.2	0.89	6.5	<0.3	<2	compact
MRC 0338–259	SB37432_component_25a	03:40:39.4	−25:47:32	QSO	0.439	371.1	590.4	0.18	5.4	<1.1	19.7	core + lobes
MRC 0418–288	SB37797_component_12a	04:20:36.4	−28:41:15	QSO	0.850	556.5	575.9	0.49	22.6	<3.2	<2	compact
MRC 0424–268	SB37797_component_3a	04:26:40.6	−26:43:45	G	0.469	1529.3	2044.5	0.58	6.3	<0.4	22.5	jets + hotspots
MRC 0450–221	SB34547_component_6a	04:52:44.7	−22:01:18	QSO	0.898	974.3	1508.0	0.23	13.2	<1.8	14.3	core + hotspots
MRC 0531–237	SB41061_component_1a	05:33:54.5	−23:44:31	G	0.851	1841.1	1913.6	0.21	6.7	143.8 ± 0.4	<2	compact
MRC 0930–200	SB34571_component_1a	09:32:45.9	−20:17:53	G	0.769	870.4	1992.2	0.21	60.0	<5.7	20.2	hotspots, no core
MRC 1002–216	SB34561_component_1a	10:05:08.3	−21:52:25	G	0.490	1364.5	1391.6	0.31	61.5	<3.7	<2	compact
MRC 2024–217	SB13372_component_4a	20:27:04.2	−21:36:19	QSO	0.459	507.4	1266.6	0.20	10.7	<1.8	31	core + hotspots
MRC 2156–245	SB10849_component_8a	21:59:24.9	−24:17:52	QSO	0.862	805.7	827.7	0.19	7.5	3.1 ± 0.3	<2	compact
MRC 2216–281	SB10849_component_1a	22:19:42.6	−27:56:27	G	0.657	3652.8	3706.3	1.91	8.2	0.3 ± 0.1	<2	compact
MRC 2255–282	SB11052_component_3a	22:58:06.0	−27:58:21	QSO	0.926	976.3	1051.9	0.18	8.7	<0.8	<1	compact
MRC 2303–253	SB11052_component_9a	23:06:26.9	−25:06:54	G	0.740	614.7	1285.0	0.15	4.3	<0.7	18.6	core + hotspots
MRC 2341–244	SB13279_component_3a	23:44:12.2	−24:07:41	G	0.590	979.7	1025.7	1.21	5.4	<0.5	2.1	compact

Notes [1, 2]: Reference for source classification: McCarthy et al. (1996); Kapahi et al. (1998a, b). References for redshifts are McCarthy et al. (1996); Kapahi et al. (1998a). Compact triple[a]: A source with a relatively bright compact core, with faint and nearly symmetric extended lobes. (e.g. Cseh, Fuhl & Frey 2008)

Table 4. The MRC 1-Jy sources observed in the FLASH pilot surveys that have multiple Gaussian components (with peak flux density >40 mJy) in the ASKAP continuum image. The columns are same as those of Table 3. The Gaussian components in various sources are labelled with alphabets [a], [b], [c] etc., appended with the MRC source name.

Source name	Component ID [FLASH]	RA	DEC	Source[1] type	Redshift[2] [z]	F_{peak} (mJy)	F_{int} (mJy)	σ_{image} (mJy)	$\sigma_{channel}$ (mJy)	τ (km s^{-1})
(1)	(2)	(3)	(4)	(5)	(6)	(7)	(8)	(9)	(10)	(11)
MRC 0042–248[a]	SB13291_component_12a	00:45:05.0	−24:34:10	QSO	0.807[a]	416.7	465.8	0.13	5.6	<1.4
MRC 0042–248[b]	SB13291_component_12b	00:45:00.7	−24:34:43	QSO	0.807[a]	145.4	187.4	0.13	5.9	<3.9
MRC 0042–248[c]	SB13291_component_12c	00:45:00.4	−24:34:47	QSO	0.807[a]	109.0	110.6	0.13	6.0	<5.1
MRC 0042–248[d]	SB13291_component_12d	00:45:04.5	−24:34:15	QSO	0.807[a]	68.9	114.3	0.13	5.7	<8.2
MRC 0058–229[a]	SB13291_component_48a	01:00:42.0	−22:39:43	QSO	0.706	190.2	423.4	0.09	5.6	<2.7
MRC 0058–229[b]	SB13291_component_48b	01:00:41.9	−22:40:28	QSO	0.706	99.3	292.6	0.09	5.7	<5.5
MRC 0123–226[a]	SB37449_component_7a	01:26:14.8	−22:22:31	QSO	0.720	767.6	804.9	0.19	7.6	<0.9
MRC 0123–226[b]	SB37449_component_7b	01:26:15.0	−22:22:36	QSO	0.720	121.9	107.9	0.19	7.4	<5.5
MRC 0135–247[a]	SB37449_component_9a	01:37:38.2	−24:30:53	QSO	0.838	590.8	645.2	0.17	18.1	<2.9
MRC 0135–247[b]	SB37449_component_9b	01:37:37.1	−24:30:54	QSO	0.838	455.7	550.7	0.17	17.7	<3.4
MRC 0135–247[c]	SB37449_component_9c	01:37:39.4	−24:30:57	QSO	0.838	91.7	108.5	0.17	18.0	<16.7
MRC 0143–246[a]	SB13281_component_15a	01:45:21.3	−24:23:54	G	0.716	387.0	433.3	0.09	4.5	<1.1
MRC 0143–246[b]	SB13281_component_15b	01:45:21.4	−24:23:06	G	0.716	204.6	306.1	0.09	4.3	<1.9
MRC 0143–246[c]	SB13281_component_15c	01:45:21.4	−24:23:46	G	0.716	72.1	139.7	0.09	4.4	<5.4
MRC 0149–299[a]	SB41226_component_3a	01:52:01.3	−29:41:00	G	0.603	504.3	493.9	0.12	6.1	<1.1
MRC 0149–299[b]	SB41226_component_3b	01:52:01.2	−29:41:03	G	0.603	384.2	438.6	0.12	6.1	<1.5
MRC 0149–299[c]	SB41226_component_3c	01:52:00.9	−29:41:00	G	0.603	305.4	401.4	0.12	6.2	<1.9
MRC 0149–299[d]	SB41226_component_3c	01:52:00.3	−29:40:51	G	0.603	264.7	235.3	0.12	6.2	<2.2
MRC 0149–299[e]	SB41226_component_3c	01:52:00.4	−29:40:58	G	0.603	79.8	81.9	0.12	6.2	<7.3
MRC 0205–229[a]	SB13268_component_20a	02:07:40.0	−22:44:50	G	0.680	351.5	579.9	0.22	6.0	<1.8
MRC 0205–229[b]	SB13268_component_20b	02:07:38.6	−22:45:05	G	0.680	324.9	558.6	0.22	6.0	<2.0
MRC 0209–282[a]	SB13268_component_11a	02:12:10.3	−28:00:17	G	0.600	431.1	454.2	0.13	5.0	<1.1
MRC 0209–282[b]	SB13268_component_11b	02:12:10.3	−28:00:07	G	0.600	236.9	256.3	0.13	5.2	<1.9
MRC 0209–282[c]	SB13268_component_11c	02:12:10.1	−28:00:02	G	0.600	155.9	140.7	0.13	5.2	<2.8
MRC 0223–245[a]	SB13268_component_7a	02:25:29.5	−24:21:15	G	0.634	577.1	569.1	0.11	4.7	<0.7
MRC 0223–245[b]	SB13268_component_7b	02:25:29.7	−24:21:19	G	0.634	150.9	130.7	0.11	4.9	<3.0
MRC 0231–235[a]	SB15212_component_8a	02:33:23.9	−23:21:14	G	0.810	807.9	1391.2	0.43	7.5	<1.0
MRC 0231–235[b]	SB15212_component_8b	02:33:25.8	−23:20:51	G	0.810	708.6	1021.8	0.43	7.7	<1.4
MRC 0254–274[a]	SB13269_component_104a	02:56:51.5	−27:18:03	G	0.480	76.1	153.0	0.11	6.1	<6.5
MRC 0254–274[b]	SB13269_component_104b	02:56:51.1	−27:17:48	G	0.480	63.5	103.1	0.11	6.2	<7.7
MRC 0254–236[a]	SB13269_component_1a	02:56:15.5	−23:24:40	G	0.509	845.6	1406.2	0.19	6.4	<0.7
MRC 0254–236[b]	SB13269_component_1b	02:56:14.3	−23:25:06	G	0.509	729.6	1161.5	0.19	6.7	<1.0
MRC 0320–267[a]	SB13269_component_3a	03:23:00.8	−26:36:14	G	0.890	681.8	724.9	0.14	7.7	<1.1
MRC 0320–267[b]	SB13269_component_3b	03:23:01.3	−26:36:11	G	0.890	58.4	50.4	0.14	7.8	<13.4
MRC 0325–260[a]	SB37432_component_57a	03:27:41.0	−25:51:28	G	0.638	168.3	182.8	0.20	6.8	<3.7
MRC 0325–260[b]	SB37432_component_57b	03:27:41.5	−25:52:24	G	0.638	86.3	112.5	0.20	6.6	<6.3
MRC 0325–260[c]	SB37432_component_57c	03:27:41.4	−25:51:40	G	0.638	43.7	93.2	0.20	6.6	<13.9
MRC 0325–260[d]	SB37432_component_57d	03:27:41.5	−25:52:10	G	0.638	40.3	97.2	0.20	6.9	<15.8
MRC 0327–241[a]	SB37432_component_6a	03:29:54.0	−23:57:08	QSO	0.895	709.2	804.3	0.48	8.3	<1.0
MRC 0327–241[b]	SB37432_component_6b	03:29:53.6	−23:57:10	QSO	0.895	147.2	161.8	0.48	8.2	<4.6
MRC 0428–281[a]	SB37797_component_8a	04:30:15.9	−28:00:48	G	0.650	609.6	634.8	0.28	7.6	<1.1
MRC 0428–281[b]	SB37797_component_8b	04:30:20.4	−28:00:39	G	0.650	503.8	542.3	0.28	7.8	<1.2
MRC 0428–281[c]	SB37797_component_8c	04:30:16.8	−28:00:48	G	0.650	138.8	205.7	0.28	7.5	<4.7
MRC 0428–281[d]	SB37797_component_8d	04:30:19.4	−28:00:41	G	0.650	101.8	154.2	0.28	7.8	<6.1
MRC 0428–271[a]	SB37797_component_13a	04:30:20.3	−27:00:01	G	0.840	503.4	546.5	0.20	8.2	<1.7
MRC 0428–271[b]	SB37797_component_13b	04:30:17.3	−26:59:49	G	0.840	356.4	389.5	0.20	8.0	<2.2
MRC 0428–271[c]	SB37797_component_13c	04:30:18.7	−26:59:54	G	0.840	63.9	105.6	0.20	8.1	<12.9
MRC 0430–235[a]	SB37797_component_67a	04:32:55.4	−23:25:20	G	0.820	129.5	152.4	0.16	7.5	<5.3
MRC 0430–235[b]	SB37797_component_67b	04:32:51.8	−23:24:08	G	0.820	117.7	132.0	0.16	7.6	<5.8
MRC 0430–235[c]	SB37797_component_67c	04:32:52.0	−23:24:17	G	0.820	93.6	142.6	0.16	7.8	<7.6
MRC 0430–235[d]	SB37797_component_67d	04:32:51.7	−23:24:26	G	0.820	79.5	116.9	0.16	7.8	<9.1

Table 4 – *continued*

Source name	Component ID [FLASH]	RA	DEC	Source[1] type	Redshift[2] [z]	F_{peak} (mJy)	F_{int} (mJy)	σ_{image} (mJy)	$\sigma_{channel}$ (mJy)	τ (km s^{-1})
(1)	(2)	(3)	(4)	(5)	(6)	(7)	(8)	(9)	(10)	(11)
MRC 0437–244[a]	SB37797_component_25a	04:39:08.3	−24:21:22	QSO	0.834	273.2	341.5	0.11	8.3	<3.0
MRC 0437–244[b]	SB37797_component_25b	04:39:10.8	−24:23:18	QSO	0.834	149.4	248.4	0.11	8.1	<4.5
MRC 0437–244[c]	SB37797_component_25c	04:39:08.8	−24:21:37	QSO	0.834	58.2	199.4	0.11	8.2	<13.2
MRC 0454–220[a]	SB34547_component_5a	04:56:12.2	−21:59:38	QSO	0.533	1207.9	1334.9	0.19	9.9	<1.2
MRC 0454–220[b]	SB34547_component_5b	04:56:07.2	−21:58:56	QSO	0.533	860.4	1018.6	0.19	9.2	<1.3
MRC 0454–220[c]	SB34547_component_5c	04:56:12.0	−21:59:35	QSO	0.533	161.9	218.1	0.19	10.2	<9.5
MRC 0454–220[d]	SB34547_component_5d	04:56:08.9	−21:59:11	QSO	0.533	128.2	112.3	0.19	8.9	<8.0
MRC 0454–220[e]	SB34547_component_5e	04:56:09.3	−21:59:15	QSO	0.533	90.3	374.8	0.19	9.2	<11.6
MRC 0522–239[a]	SB41061_component_20a	05:24:54.0	−23:52:20	G	0.500	206.5	279.9	0.15	5.4	<2.2
MRC 0522–239[b]	SB41061_component_20b	05:24:54.6	−23:52:15	G	0.500	184.2	218.2	0.15	5.4	<2.4
MRC 0522–239[c]	SB41061_component_20c	05:24:53.5	−23:52:25	G	0.500	150.3	158.7	0.15	5.3	<3.0
MRC 0941–200[a]	SB34571_component_24a	09:43:50.4	−20:19:41	QSO	0.715	287.3	437.6	0.09	7.9	<3.1
MRC 0941–200[b]	SB34571_component_24b	09:43:50.3	−20:19:01	QSO	0.715	86.9	216.7	0.09	7.6	<9.7
MRC 1002–215[a]	SB34561_component_6a	10:05:11.4	−21:45:09	G	0.589	1043.7	1241.2	0.38	64.1	<5.1
MRC 1002–215[b]	SB34561_component_6b	10:05:11.6	−21:44:41	G	0.589	1008.8	1278.9	0.38	71.5	<5.9
MRC 2201–272[a]	SB10849_component_7a	22:04:35.1	−27:01:17	G	0.930	865.6	929.8	0.31	7.3	<0.8
MRC 2201–272[b]	SB10849_component_7b	22:04:34.8	−27:01:24	G	0.930	58.8	45.3	0.31	7.3	<10.5
MRC 2213–283[a]	SB10849_component_10a	22:16:03.0	−28:03:31	QSO	0.948	499.2	552.7	0.25	7.9	<1.5
MRC 2213–283[b]	SB10849_component_10b	22:15:58.9	−28:03:30	QSO	0.948	476.4	489.6	0.25	8.4	<1.7
MRC 2213–283[c]	SB10849_component_10c	22:15:59.6	−28:03:30	QSO	0.948	124.4	170.9	0.25	8.2	<6.6
MRC 2213–283[d]	SB10849_component_10d	22:16:02.2	−28:03:29	QSO	0.948	93.6	192.8	0.25	8.3	<8.7
MRC 2229–228[a]	SB11051_component_5a	22:32:05.5	−22:33:41	G	0.542	343.1	305.8	0.60	5.5	<1.3
MRC 2229–228[b]	SB11051_component_5b	22:32:05.9	−22:33:43	G	0.542	211.5	195.5	0.60	5.4	<2.1
MRC 2229–228[c]	SB11051_component_5c	22:32:05.7	−22:33:37	G	0.542	178.1	189.7	0.60	5.4	<2.5
MRC 2229–228[d]	SB11051_component_5d	22:32:05.1	−22:33:43	G	0.542	70.8	41.7	0.60	5.5	<6.5
MRC 2232–232[a]	SB11051_component_3a	22:35:20.5	−22:59:42	G	0.870	914.7	1001.4	0.18	6.8	<0.7
MRC 2232–232[b]	SB11051_component_3b	22:35:19.6	−22:59:53	G	0.870	315.4	318.1	0.18	6.9	<2.3
MRC 2236–264[a]	SB11051_component_27a	22:39:20.3	−26:10:18	G	0.430	171.9	270.9	0.21	4.2	<2.0
MRC 2236–264[b]	SB11051_component_27b	22:39:19.1	−26:09:57	G	0.430	88.9	204.0	0.21	4.3	<4.0
MRC 2236–264[c]	SB11051_component_27c	22:39:19.9	−26:10:08	G	0.430	57.8	146.3	0.21	4.3	<6.1
MRC 2236–264[d]	SB11051_component_27d	22:39:20.5	−26:10:16	G	0.430	56.9	62.3	0.21	4.2	<6.1
MRC 2240–260[a]	SB11051_component_2a	22:43:26.3	−25:44:30	QSO	0.774	731.4	775.0	0.22	5.2	<0.7
MRC 2240–260[b]	SB11051_component_2b	22:43:26.5	−25:44:28	QSO	0.774	374.9	437.7	0.22	5.3	<1.3
MRC 2240–260[c]	SB11051_component_2c	22:43:26.2	−25:44:30	QSO	0.774	51.6	121.1	0.22	5.2	<10.0
MRC 2254–248[a]	SB11052_component_2a	22:57:40.2	−24:37:33	G	0.540	949.6	973.0	0.17	4.3	<0.4
MRC 2254–248[b]	SB11052_component_2b	22:57:40.2	−24:37:28	G	0.540	195.4	179.5	0.17	4.3	<2.0
MRC 2254–248[c]	SB11052_component_2c	22:57:41.7	−24:37:41	G	0.540	49.5	67.4	0.17	4.4	<8.0
MRC 2311–222[a]	SB11052_component_4a	23:14:39.0	−21:55:54	G	0.434	893.2	942.0	0.25	7.7	<0.7
MRC 2311–222[b]	SB11052_component_4b	23:14:33.6	−21:55:55	G	0.434	136.8	218.6	0.25	7.8	<4.4
MRC 2311–222[c]	SB11052_component_4c	23:14:37.6	−21:55:54	G	0.434	52.0	184.5	0.25	7.7	<11.6
MRC 2313–277[a]	SB11052_component_11a	23:16:18.9	−27:29:51	G	0.614	507.6	590.4	0.16	6.6	<1.1
MRC 2313–277[b]	SB11052_component_11b	23:16:21.9	−27:30:02	G	0.614	231.0	243.8	0.16	6.6	<2.3
MRC 2313–277[c]	SB11052_component_11c	23:16:20.8	−27:30:00	G	0.614	129.9	262.8	0.16	6.4	<3.6
MRC 2313–277[d]	SB11052_component_11d	23:16:19.7	−27:29:53	G	0.614	80.1	92.8	0.16	6.7	<6.8
MRC 2338–290[a]	SB13279_component_56a	23:40:51.8	−28:48:03	QSO	0.449	124.4	166.8	0.20	16.3	<10.6
MRC 2338–290[b]	SB13279_component_56b	23:40:49.7	−28:49:00	QSO	0.449	74.7	180.9	0.20	16.9	<20.1
MRC 2338–290[c]	SB13279_component_56c	23:40:48.9	−28:49:05	QSO	0.449	65.2	92.6	0.20	16.7	<22.5
MRC 2338–290[d]	SB13279_component_56d	23:40:50.8	−28:48:48	QSO	0.449	49.6	188.4	0.20	16.8	<30.1
MRC 2338–233[a]	SB13279_component_14a	23:40:45.6	−23:02:53	QSO	0.715	386.0	451.9	0.12	6.3	<1.6
MRC 2338–233[b]	SB13279_component_14b	23:40:45.3	−23:02:27	QSO	0.715	196.0	230.7	0.12	6.5	<3.2
MRC 2340–219[a]	SB13279_component_16a	23:43:24.2	−21:41:46	G	0.766	344.3	394.4	0.23	12.1	<3.7
MRC 2340–219[b]	SB13279_component_16b	23:43:24.1	−21:41:21	G	0.766	263.6	290.6	0.23	12.0	<4.1
MRC 2340–219[c]	SB13279_component_16c	23:43:24.2	−21:41:31	G	0.766	159.6	278.2	0.23	12.2	<8.2
MRC 2343–243[a]	SB10850_component_13a	23:45:46.8	−24:02:15	G	0.600	351.1	366.4	0.24	7.7	<2.2
MRC 2343–243[b]	SB10850_component_13b	23:45:43.8	−24:02:41	G	0.600	274.1	307.5	0.24	7.7	<2.7

Table 4 – *continued*

Source name	Component ID [FLASH]	RA	DEC	Source[1] type	Redshift[2] [z]	F_{peak} (mJy)	F_{int} (mJy)	σ_{image} (mJy)	$\sigma_{channel}$ (mJy)	τ (km s^{-1})
(1)	(2)	(3)	(4)	(5)	(6)	(7)	(8)	(9)	(10)	(11)
MRC 2343–243[c]	SB10850_component_13c	23:45:46.0	−24:02:17	G	0.600	109.9	165.1	0.24	7.9	<7.2
MRC 2343–243[d]	SB10850_component_13d	23:45:44.9	−24:02:34	G	0.600	108.6	205.8	0.24	8.3	<6.7
MRC 2348–235[a]	SB10850_component_14a	23:51:28.3	−23:17:33	G	0.952	365.9	554.5	0.22	8.1	<2.2
MRC 2348–235[b]	SB10850_component_14b	23:51:28.0	−23:16:37	G	0.952	296.7	373.0	0.22	7.7	<2.3

Notes. [1,2]: References for source classification: McCarthy et al. (1996); Kapahi et al. (1998a, b). References for redshift: McCarthy et al. (1996); Kapahi et al. (1998b). Notes [a,b]: for MRC 0042–248 and MRC 0055–258 the redshift references are Pocock et al. (1984) and Brown, Webster & Boyle (2001), respectively.

the fits, the residual was consistent with noise. Among these, the peak of the stronger component is blueshifted by ≈ 73 km s^{-1}, and the weaker component is marginally redshifted by ≈ 12.6 km s^{-1} w.r.t the AGN redshift of $z = 0.851$. The absorption could be arising either from a few, or all, of the compact and diffuse components visible in the 8.4 GHz VLBI image. The optical depths of various absorption components could be added up in velocity domain, giving rise to the observed absorption profile. Among associated H I 21-cm absorbers the detection fraction is known to be relatively higher in low redshift compact peaked-spectrum sources (Gupta et al. 2006; Aditya & Kanekar 2018a), a reason for which could be higher gas covering factor due to compact background emission in these systems. Given that the total extension of emission at 8.4 GHz is only ≈465 pc, and that the typical size of the H I cloud could be ≈100 pc (see e.g. Braun 2012) which accounts to a significant fraction of the size of the emission, it is likely that the complete radio emission is obscured by neutral gas.

The blueshifted absorption wing in Fig. 3(c) (bottom-left panel) extends up to ≈ 431 km s^{-1} at the null, indicative of gas outflows. However, given that an uncertainty on AGN redshift is not available, we cannot confirm the presence of outflows. The absorption has a total width of ≈ 662.9 km s^{-1} at the nulls. While a majority of narrow absorption features with widths $\lesssim$ 200 km s^{-1} are known to be arising from rotating disc-like gaseous structures around the nucleus (Maccagni et al. 2017; Murthy et al. 2021), wider features are thought to created by shocks and turbulences resulting from strong jet–gas interactions. The likely scenario of the radio emission being embedded in a dense medium is consistent with a situation where strong interactions between the ambient gas and the expanding jets could be taking place.

5.1.1 H I gas density and OH upper limits

The physical conditions of the atomic and molecular gases in AGN vicinities could be drastically different from those in the Galactic clouds. Strong accretion to the nuclear regions, and, the kinematic feedback from the AGN jets could be significantly affecting the gas densities. Beyond the local Universe ($z > 1.0$), currently there are limited number of studies that have probed the H I gas densities, estimated through H I 21-cm absorption at high spatial resolution (e.g. Araya et al. 2010; Morganti et al. 2013). Morganti et al. (2013) have reported densities of $150 - 300$ cm^{-3} in the nuclear regions of 4C12.50 (at $z = 0.12174$), while Araya et al. (2010) have estimated densities of $10^2 - 10^3$ cm^{-3} in B2352+495 (at $z = 0.2379$).

We estimate a gas density of ≈ 85 cm^{-3}, based on $N_{HI} = (2.62 \pm 0.01) \times 10^{22}$ cm^{-2}, assuming $T_s = 100$ K. Further, we conservatively assume that the H I gas is uniformly distributed across the radio emission of size ≈ 97 pc × 465 pc (in the 8.4 GHz VLBI image, and assume a scale of 100 pc; e.g. Braun 2012) for the gas clouds, which is similar to the width of the projected radio emission along the line of sight. We note that a spin temperature of $T_s = 100$ K is only a fiducial value, used for a comparison of the column density with literature estimates. For the gas present in close vicinities of the radio AGN, as in the present case, the values could be as high as 1000–8000 K (e.g. Maloney, Hollenbach & Tielens 1996; Araya et al. 2010). Or, the temperature could be lower than 100 K, in dense isolated clouds. The density would vary significantly depending on the assumed spin temperature. Also, for a localized and clumpy distribution of H I gas, and higher spin temperatures, the gas density could be higher than our estimate, even by an order of magnitude. The fiducial estimate of gas density appears to be higher than the densities of cold H I clouds (≈ 30 cm^{-3}) found in our Galaxy, and, is comparable to the densities of diffuse molecular gas clouds (≈ 100 cm^{-3}), where abundant H_2 molecules could be present in the cloud interiors (Draine 2011).

We did not detect any OH 1665 or 1667 MHz lines in our ASKAP spectrum (see Fig. 3d). By using the expression

$$N_{OH} = T_{ex} \times C_o \times \int \tau_{1667} dv \, ,$$

where $C_o = 2.2 \times 10^{14}$ cm^{-2} K^{-1}(km s^{-1})$^{-1}$ for the 1667 MHz line, and $T_{ex} = 8$ K (upper limit for excitation temperature in Galactic diffuse clouds; Dickey, Crovisier & Kazes 1981), we estimate a 3σ upper limit of $N_{OH} < 1.6 \times 10^{14}$ cm^{-2} for the OH column density. The OH column densities in the Galactic diffuse clouds are known to be typically of the order of $N_{OH} \sim 10^{14}$ cm^{-2}, while in the dense molecular clouds they are $N_{OH} \sim 10^{16}$ cm^{-2} (e.g. Dickey, Crovisier & Kazes 1981; Gupta et al. 2018). Our upper limit is stringent enough to rule out the presence of any dense molecular clouds, while it is comparable to the column density of diffuse clouds. However, we note that while the OH excitation temperature is weakly dependent on the gas kinetic temperature, and thus, on the H I spin temperature, proximity of the gas to the radio jets could raise the excitation temperature significantly (Dickey, Crovisier & Kazes 1981), yielding a low optical depth for a given column density. Also, the gas covering factor could be playing a critical role here; the localized distribution of molecular gas within the H I cloud would mean that it would have a small covering factor against the background radio emission, making it difficult to detect in absorption.

5.2 MRC 2156–245

Baker et al. (1999) reported detections of [Ne V], H β, Mg II, [O II], and H γ lines in the optical observations towards the source. They reported a redshift of $z = 0.862$ for the source, which is the average of the estimates for individual lines. We conservatively estimate an uncertainty of 0.003 on redshift, which is the separation between H γ and the redshift average.

Table 5. MRC 1-Jy sources observed in the FLASH pilot surveys for which measurements of interplanetary scintillation (IPS) are also available.

GLEAM name	S_{162} (Jy)	MRC name	Type	z	FLASH components	NSI_fit IPS	NSI_err IPS	LAS_{5GHz} (arcsec)
(1)	(2)	(3)	(4)	(5)	(6)	(7)	(8)	(9)
J003244-214414	1.79	MRC 0030–220	Q	0.806	1	0.204	0.014	3.9
J003824-225256	2.33	MRC 0035–231	G	0.685	1	0.371	0.025	2.3
J004503-243417	2.64	MRC 0042–248	Q	0.807	4	0.067	0.010	73
J005242-215540	2.45	MRC 0050–222	G	0.654	1	0.559	0.037	<2
J010041-223955	2.61	MRC 0058–229	Q	0.706	2	<0.030	..	63
J010902-230728	1.94	MRC 0106–233	Q	0.818	1	0.435	0.031	2.5
J012031-270125	1.87	MRC 0118–272	Q	>0.557	1	0.294	0.039	<2
J012614-222227	2.57	MRC 0123–226	Q	0.720	2	0.169	0.013	5.1
J013737-243048	3.76	MRC 0135–247	Q	0.838	3	0.215	0.016	<2
J014521-242333	3.12	MRC 0143–246	G	0.716	3	0.217	0.018	52.5
J014709-223234	1.98	MRC 0144–227	G	0.600	1	0.618	0.013	<2
J020332-211342	1.02	MRC 0201–214	G	0.915	1	0.886	0.059	<2
J020739-224454	3.25	MRC 0205–229	G	0.680	2	0.056	0.010	34.4
J021128-232819	2.59	MRC 0209–237	Q	0.680	1	0.087	0.012	18
J021209-280009	2.68	MRC 0209–282	G	0.600	3	<0.107	..	13.3
J022529-242113	1.62	MRC 0223–245	G	0.634	2	0.925	0.066	<1
J022733-235450	4.05	MRC 0225–241	G	0.520	1	0.076	0.007	5.2
J023230-242201	4.05	MRC 0230–245	G	0.880	1	0.148	0.011	11.3
J023324-232059	8.56	MRC 0231–235	G	0.810	2	0.067	0.005	38.4
J023556-285044	4.01	MRC 0233–290	G	0.725	1	0.245	0.026	<5
J025614-232447	12.95	MRC 0254–236	G	0.509	2	0.032	0.002	33.4
J025651-271756	2.54	MRC 0254–274	G	0.480	2	0.086	0.023	37.4
J032300-263613	1.54	MRC 0320–267	G	0.890	2	0.302	0.037	4.3
J032741-255151	1.45	MRC 0325–260	G	0.638	4	<0.062	..	59
J032954-235707	2.25	MRC 0327–241	Q	0.895	2	0.104	0.019	<2
J034039-254734	2.01	MRC 0338–259	Q	0.439	1	<0.092	..	19.7
J043252-232432	1.92	MRC 0430–235	G	0.820	4	<0.118	..	91
J043909-242155	2.64	MRC 0437–244	Q	0.834	3	<0.063	..	126
J045244-220117	6.55	MRC 0450–221	Q	0.898	1	0.091	0.011	14.3
J045610-215922	8.00	MRC 0454–220	Q	0.533	5	0.054	0.008	84
J052454-235214	1.81	MRC 0522–239	G	0.500	3	<0.154	..	23.4
J093245-201750	6.28	MRC 0930–200	G	0.769	1	0.136	0.009	20.2
J094350-201929	2.12	MRC 0941–200	Q	0.715	2	0.054	0.013	47.7
J100507-215221	2.52	MRC 1002–216	G	0.490	1	0.784	0.058	<2
J100511-214451	16.12	MRC 1002–215	G	0.589	2	0.034	0.003	29.1
J202704-213616	3.97	MRC 2024–217	Q	0.459	1	0.076	0.005	31
J215924-241751	1.95	MRC 2156–245	Q	0.862	1	0.795	0.051	<2
J220435-270119	2.73	MRC 2201–272	G	0.930	2	0.319	0.024	5.8
J221600-280329	5.82	MRC 2213–283	Q	0.948	4	0.038	0.004	58
J221942-275626	9.46	MRC 2216–281	G	0.657	1	0.823	0.072	<2
J223205-223339	1.90	MRC 2229–228	G	0.542	4	0.594	0.046	6.6
J223520-225946	3.27	MRC 2232–232	G	0.870	2	0.266	0.020	15
J223919-261008	1.91	MRC 2236–264	G	0.430	4	<0.026	..	25.7
J224326-254429	2.38	MRC 2240–260	Q	0.774	3	0.283	0.020	11
J225740-243728	2.56	MRC 2254–248	G	0.549	3	0.380	0.027	25
J225805-275818	1.29	MRC 2255–282	Q	0.926	1	0.204	0.018	<1
J230627-250653	5.70	MRC 2303–253	G	0.740	1	0.112	0.009	18.6
J231438-215552	3.59	MRC 2311–222	G	0.434	3	0.218	0.017	80
J231620-272953	3.87	MRC 2313–277	G	0.614	4	0.073	0.007	44.2
J234045-230243	1.53	MRC 2338–233	Q	0.715	2	0.096	0.011	19.5
J234045-230243	1.53	MRC 2338–290	Q	0.449	4	<0.013	..	73
J234324-214129	4.52	MRC 2340–219	G	0.766	3	0.052	0.004	27.1
J234412-240744	2.20	MRC 2341–244	G	0.590	1	0.466	0.035	2.1
J234545-240232	3.66	MRC 2343–243	G	0.600	4	0.074	0.006	48.3
J235128-231708	2.82	MRC 2348–235	G	0.952	2	<0.035	..	68.7

Table 6. Peaked-spectrum and compact steep-spectrum sources from the MRC 1-Jy sample observed in the FLASH pilot survey.

MRC name	z	Type	FLASH components	$\nu_{\rm peak,\ obs.}$ (MHz)	Notes
(1)	(2)	(3)	(4)	(5)	(6)
(i) Peaked-spectrum sources					
MRC 0201–214	0.915	G	1	267.6	
MRC 0223–245	0.634	G	2	213.7	
MRC 0531–237	0.851	G	1	610.6	H I absorption detected
MRC 2216–281	0.657	G	1	161.9	H I absorption detected
(ii) Compact steep-spectrum (CSS) sources					
MRC 0035–231	0.685	G	1	..	
MRC 0050–222	0.654	G	1	..	
MRC 0144–227	0.600	G	1	..	
MRC 0233–290	0.725	G	1	..	
MRC 0319–298	0.583	G	1	..	
MRC 0418–288	0.850	QSO	1	..	
MRC 1002–216	0.490	G	1	..	
MRC 2156–245	0.862	QSO	1	..	H I absorption detected
MRC 2341–244	0.590	G	1	..	

The radio source is unresolved in the ASKAP continuum image at 856 MHz, with a peak flux density of 805.7 mJy (see Fig. 4a). The SED fit to radio flux measurements at frequencies 70 MHz to 11 GHz is shown in Fig. 4(b), which has an overall steep shape. The steep spectral shape due to synchrotron energy losses at high frequencies, indicates that the radio sources could have an extended structure at smaller scales.

We have detected H I 21-cm absorption in our ASKAP observations, against the peak of the radio source (Fig. 4c). While the line peak is weak in comparison to the noise (for MRC 2156–245, and MRC 2216–281; see the next section), we note that we do not find any radio-frequency interference (RFI) or band corruptions in the spectra of other sources within the beam, observed in the SBID corresponding to this target. The absorption has a velocity-integrated optical depth of 3.12 ± 0.33 km s^{-1}, implying that the detection has a significance of 9.5σ.

We estimate a column density of $(5.69 \pm 0.60) \times 10^{20}$ cm^{-2}, assuming a spin temperature of 100 K, and a unity covering factor. The peak of the absorption is redshifted from the source redshift ($z = 0.862$) by ≈ 955 km s^{-1}. However, given the large uncertainty on the redshift, we cannot confirm the gas kinematics.

5.3 MRC 2216–281

McCarthy et al. (1996) have reported an optical spectroscopic redshift of $z = 0.657 \pm 0.050$ for the source. To investigate the large uncertainty on the redshift, we downloaded the archival data of the optical observations conducted using Anglo-Australian Telescope (AAT) during 1989–1993. However, we find that the quality of the data is relatively poor. Our efforts on calibration and subsequent data reduction, to identify the optical emission/absorption lines, were not successful.

The radio source is unresolved in the ASKAP image at ≈856 MHz, and the peak flux density of the radio source is 3652.8 mJy. The radio frequency SED has a slight turnover at ∼110 MHz as shown in Fig. 5(b) (see also Section 6.3).

We have detected a narrow H I 21-cm absorption line towards the source as shown in Fig. 5(c), where the line peak has a redshift of $z = 0.6260$. The large uncertainty (≈ 14 000 km s^{-1} in velocity) on the redshift implies that it is not possible to assess whether the absorption is associated with the source, or if it is arising from a lower redshift gas cloud that is intervening our line of sight. The line has a width of 40.7 km s^{-1} at the nulls, and a velocity-integrated optical depth of 0.26 ± 0.04 km s^{-1}, implying a column density of $(4.74 \pm 0.07) \times 10^{19}$ cm^{-2}. It is interesting to note a recent detection at $z \approx 0.7$ by Mahony et al. (2022), which also has a similarly large difference between the H I peak and the AGN redshift. Here, the H I is detected against the radio lobe of PKS 0409–75, which is not associated with the source but arises from gas in the same galaxy group.

MRC 2216–281 is the only one of our three H I-detected sources with a published X-ray detection (J221942.6–275627 in the 4XMM-DR13 catalogue; Webb et al. 2020). Assuming a suitable K correction for a power-law index $\Gamma = 1.7$ gives a rest-frame X-ray luminosity L(2–10 keV) $= 3.5\ (\pm 1.0) \times 10^{43}$ erg s^{-1}.

6 DISCUSSION

6.1 Detection fraction

As discussed above, our sample is unbiased in terms of radio source properties, and covers the intermediate redshift range of $0.42 < z < 1.00$. To compare the detection fraction in our sample with other studies in the literature, we smoothed the spectra of non-detections to a velocity resolution of 100 km s^{-1} and estimated the 3σ upper limits to the velocity integrated optical depth, $\int \tau {\rm d}V$, assuming a line width of 100 km s^{-1}. Here, the assumed line width of 100 km s^{-1} is used as a conventional value to compare the optical depth sensitivity in various literature samples. A number of earlier studies have used this velocity (e.g. Vermeulen et al. 2003; Aditya, Kanekar & Kurapati 2016; Aditya & Kanekar 2018b) for the assumed H I 21-cm line width in estimating the optical depth sensitivity; therefore it is reasonable to compare the optical depth sensitivities at 100 km s^{-1} in various samples.

The median 3σ limit on the integrated optical depth in our sample, for the radio components that are closest to their *wide-field infrared survey explorer* (*WISE*) counterparts, is < 2.07 km s^{-1}. Five sources in our sample have shallow upper limits (due to poor spectra with large noise) in the range of $12 - 30$ km s^{-1}, which are ≈6–15 times the median value, making them outliers in the sample; we hence

Table 7. Luminosities and *WISE* colours for the sample. The columns are: (1) the source name, (2) the FLASH component ID, (3) the source right ascension, (4) the source declination, (5) the source redshift, z, (6) the logarithm of rest-frame 1.4 GHz luminosity, $L'_{rad} = \log_{10}(L_{1.4\ GHz}/W\ Hz^{-1})$, (7) the logarithm UV luminosity at 1216 Å, $L'_{UV} = \log_{10}(L_{UV}/W\ Hz^{-1})$ (8) the logarithm of UV ionizing photon rate, $Q'_{UV} = Q' = \log_{10}Q/s^{-1}$, (9) & (10), (11) & (12) and (13) & (14) the *WISE* fluxes in mag., in the W1, W2, and W3 bands, and their uncertainties, eW1, eW2, and eW3, respectively.

Source name	Component ID [FLASH]	RA	DEC	Redshift [z]	L'_{rad}	L'_{UV}	Q'_{UV}	W1 mag	eW1 mag	W2 mag	eW2 mag	W3 mag	eW3 mag
(1)	(2)	(3)	(4)	(5)	(6)	(7)	(8)	(9)	(10)	(11)	(12)	(13)	(14)
MRC 0030–220	SB11053_component_10a	00:32:44.6	−21:44:21	0.806	26.90	–	–	15.612	0.049	14.886	0.075	11.955	0.298
MRC 0035–231	SB11053_component_6a	00:38:24.9	−22:53:03	0.685	26.92	<22.40	<55.53	15.470	0.043	15.317	0.093	>12.526	–
MRC 0042–248	SB13291_component_12d	00:45:05.0	−24:34:10	0.807	26.07	–	–	16.855	0.104	17.097	0.504	>12.440	–
MRC 0050–222	SB13291_component_7a	00:52:42.8	−21:55:47	0.654	26.87	22.12	56.95	15.635	0.045	15.455	0.105	11.046	0.127
MRC 0058–229	SB13291_component_48a	01:00:42.0	−22:39:43	0.706	26.39	–	–	15.658	0.046	15.477	0.104	12.594	0.476
MRC 0106–233	SB13291_component_9a	01:09:02.9	−23:07:30	0.818	26.98	20.97	53.58	14.920	0.035	14.227	0.045	10.879	0.112
MRC 0118–272	SB37449_component_5a	01:20:31.5	−27:01:23	0.559	26.99	23.19	56.24	11.316	0.022	10.385	0.020	7.761	0.020
MRC 0123–226	SB37449_component_7b	01:26:14.8	−22:22:31	0.720	26.22	23.08	56.36	13.877	0.026	12.844	0.028	10.201	0.083
MRC 0135–247	SB13281_component_5a	01:37:38.2	−24:30:53	0.838	27.10	23.75	57.39	12.920	0.024	11.744	0.022	8.650	0.022
MRC 0143–246	SB13281_component_15c	01:45:21.3	−24:23:54	0.716	25.98	21.67	54.56	16.842	0.101	16.897	0.384	>12.633	–
MRC 0144–227	SB37475_component_6a	01:47:09.2	−22:32:41	0.600	26.81	–	–	15.733	0.045	15.327	0.094	>12.185	–
MRC 0149–299	SB35939_component_2b	01:52:01.2	−29:41:02	0.603	26.53	–	–	15.137	0.033	14.468	0.045	11.855	0.174
MRC 0201–214	SB13268_component_15a	02:03:32.1	−21:13:46	0.915	26.97	–	–	16.012	0.049	15.558	0.094	11.832	0.184
MRC 0205–229	SB13268_component_20a	02:07:40.0	−22:44:50	0.680	26.63	<23.15	<56.68	16.473	0.140	16.247	0.264	>12.198	–
MRC 0209–237	SB13268_component_12a	02:11:28.3	−23:28:23	0.680	26.69	–	–	14.364	0.028	13.509	0.031	10.951	0.104
MRC 0209–282	SB34584_component_18a	02:12:10.3	−28:00:17	0.600	26.69	–	–	15.705	0.041	15.691	0.111	>12.889	–
MRC 0223–245	SB13268_component_7a	02:25:29.5	−24:21:15	0.634	26.78	–	–	15.898	0.049	16.025	0.170	>11.981	–
MRC 0225–241	SB15212_component_4a	02:27:33.5	−23:54:55	0.520	26.88	21.27	54.15	14.813	0.029	14.215	0.042	11.926	0.201
MRC 0230–245	SB15212_component_5a	02:32:30.4	−24:22:05	0.880	27.27	–	–	15.943	0.043	15.465	0.081	12.058	0.22
MRC 0231–235	SB15212_component_8a	02:33:23.9	−23:21:14	0.810	27.14	<21.67	<54.50	16.372	0.054	15.881	0.103	12.758	0.417
MRC 0233–290	SB37451_component_1a	02:35:56.2	−28:50:46	0.725	27.14	–	–	15.811	0.044	15.466	0.092	12.259	0.299
MRC 0254–236	SB15212_component_6d	02:56:15.5	−23:24:40	0.509	26.16	–	–	16.593	0.067	16.361	0.182	>12.975	–
MRC 0254–274	SB13269_component_104a	02:56:51.5	−27:18:03	0.480	25.65	<20.93	<53.90	15.7	0.102	15.540	0.149	>12.258	–
MRC 0319–298	SB37452_component_1a	03:21:28.8	−29:40:45	0.583	27.40	–	–	13.970	0.026	12.851	0.025	9.566	0.033
MRC 0320–267	SB13269_component_3a	03:23:00.8	−26:36:14	0.890	27.15	–	–	16.644	0.064	16.582	0.193	>12.614	–
MRC 0325–260	SB37432_component_57c	03:27:41.0	−25:51:28	0.638	25.66	–	–	13.303	0.024	13.206	0.026	>12.600	–
MRC 0327–241	SB37432_component_6a	03:29:54.0	−23:57:08	0.895	27.17	22.16	54.80	14.869	0.030	13.840	0.032	10.910	0.080
MRC 0338–259	SB37432_component_25a	03:40:39.4	−25:47:32	0.439	26.26	–	–	16.378	0.057	15.537	0.086	12.647	0.520
MRC 0418–288	SB37797_component_12a	04:20:36.4	−28:41:15	0.850	27.02	–	–	14.507	0.030	13.436	0.031	10.595	0.073
MRC 0424–268	SB37797_component_3a	04:26:40.6	−26:43:45	0.469	26.93	–	–	14.896	0.035	14.754	0.058	>12.616	–
MRC 0428–271	SB37797_component_13c	04:30:20.3	−27:00:01	0.840	26.07	–	–	15.493	0.040	15.376	0.084	>12.374	–
MRC 0428–281	SB37797_component_8d	04:30:15.9	−28:00:48	0.650	26.05	–	–	14.990	0.032	14.628	0.051	10.634	0.083
MRC 0430–235	SB37797_component_67d	04:32:55.4	−23:25:20	0.820	26.15	–	–	16.157	0.055	<16.721	–	>12.635	–
MRC 0437–244	SB37797_component_25c	04:39:08.3	−24:21:22	0.834	26.03	–	–	15.358	0.038	15.369	0.083	>12.244	–
MRC 0450–221	SB34547_component_6a	04:52:44.7	−22:01:18	0.898	27.31	<22.65	<55.68	13.784	0.025	12.639	0.023	9.664	0.036
MRC 0454–220	SB34547_component_5d	04:56:12.2	−21:59:38	0.533	25.97	23.91	57.69	15.653	0.034	15.636	0.079	>12.312	–

Table 7 – *continued*

Source name	Component ID [FLASH]	RA	DEC	Redshift [z]	L'_{rad}	L'_{UV}	Q'_{UV}	W1 mag	eW1 mag	W2 mag	eW2 mag	W3 mag	eW3 mag
(1)	(2)	(3)	(4)	(5)	(6)	(7)	(8)	(9)	(10)	(11)	(12)	(13)	(14)
MRC 0522–239	SB34570_component_21a	05:24:53.8	−23:52:21	0.500	26.17	–	–	15.605	0.041	15.217	0.076	>12.680	–
MRC 0531–237	SB34570_component_1a	05:33:54.5	−23:44:31	0.851	27.54	–	–	15.556	0.042	15.151	0.074	>12.259	–
MRC 0930–200	SB34571_component_1a	09:32:45.9	−20:17:53	0.769	27.13	–	–	14.930	0.033	14.193	0.042	11.658	0.212
MRC 0941–200	SB34571_component_24a	09:43:50.4	−20:19:41	0.715	26.58	22.53	55.25	15.397	0.060	15.020	0.097	>11.382	–
MRC 1002–215	SB34561_component_6b	10:05:11.4	−21:45:09	0.589	26.96	–	–	15.468	0.041	15.329	0.087	>12.208	–
MRC 1002–216	SB34561_component_1a	10:05:08.3	−21:52:25	0.490	26.92	–	–	15.475	0.042	15.168	0.088	>12.603	–
MRC 2024–217	SB13372_component_4a	20:27:04.2	−21:36:19	0.459	26.43	21.30	54.25	14.411	0.031	13.376	0.033	10.890	0.140
MRC 2156–245	SB10849_component_8a	21:59:24.9	−24:17:52	0.862	27.20	–	–	14.549	0.031	13.486	0.033	10.283	0.078
MRC 2201–272	SB10849_component_7a	22:04:35.1	−27:01:17	0.930	27.29	–	–	15.954	0.053	16.293	0.226	>12.301	–
MRC 2213–283	SB10849_component_10c	22:16:03.0	−28:03:31	0.948	26.47	<23.56	<56.97	14.301	0.029	14.036	0.042	11.634	0.240
MRC 2216–281	SB10849_component_1a	22:19:42.6	−27:56:27	0.657	27.61	–	–	15.432	0.041	15.297	0.098	>11.750	–
MRC 2229–228	SB11051_component_5b	22:32:05.5	−22:33:41	0.542	26.20	–	–	15.720	0.050	14.906	0.070	10.758	0.101
MRC 2232–232	SB11051_component_3a	22:35:20.5	−22:59:42	0.870	27.26	–	–	15.503	0.047	13.913	0.042	9.626	0.045
MRC 2236–264	SB11051_component_27c	22:39:20.3	−26:10:18	0.430	25.43	<20.26	<52.95	14.110	0.029	13.438	0.034	11.041	0.126
MRC 2240–260	SB11051_component_2a	22:43:26.3	−25:44:30	0.774	27.06	22.41	55.50	12.054	0.022	11.087	0.021	8.574	0.027
MRC 2254–248	SB11052_component_2a	22:57:40.2	−24:37:33	0.540	26.85	–	–	14.696	0.032	13.667	0.038	10.646	0.093
MRC 2255–282	SB11052_component_3a	22:58:06.0	−27:58:21	0.926	27.34	<23.73	<56.92	11.963	0.023	10.846	0.021	7.864	0.021
MRC 2303–253	SB11052_component_9a	23:06:26.9	−25:06:54	0.740	26.94	–	–	15.710	0.049	15.157	0.089	11.742	0.243
MRC 2311–222	SB11052_component_4c	23:14:39.0	−21:55:54	0.434	25.39	21.31	54.11	16.450	0.075	16.663	0.331	>12.317	–
MRC 2313–277	SB11052_component_11c	23:16:18.9	−27:29:51	0.614	26.10	<22.80	<55.64	16.116	0.059	16.349	0.229	12.252	0.351
MRC 2338–233	SB13279_component_14b	23:40:45.6	−23:02:53	0.715	26.42	<23.20	<56.63	13.749	0.026	12.630	0.024	10.044	0.056
MRC 2338–290	SB13279_component_56d	23:40:49.7	−28:49:00	0.449	25.41	21.83	55.23	17.464	0.155	16.790	0.338	>12.479	–
MRC 2340–219	SB13279_component_16c	23:43:24.2	−21:41:46	0.766	26.39	–	–	15.097	0.036	15.305	0.092	>12.143	–
MRC 2341–244	SB13279_component_3a	23:44:12.2	−24:07:41	0.590	26.95	<21.49	<54.35	15.209	0.038	14.973	0.078	>11.946	–
MRC 2343–243	SB13279_component_17d	23:45:46.8	−24:02:15	0.600	25.80	<22.29	<55.29	16.087	0.061	16.076	0.185	>12.196	–
MRC 2348–235	SB10850_component_14a	23:51:28.3	−23:17:33	0.952	26.94	–	–	17.644	0.202	<16.551	–	>12.149	–

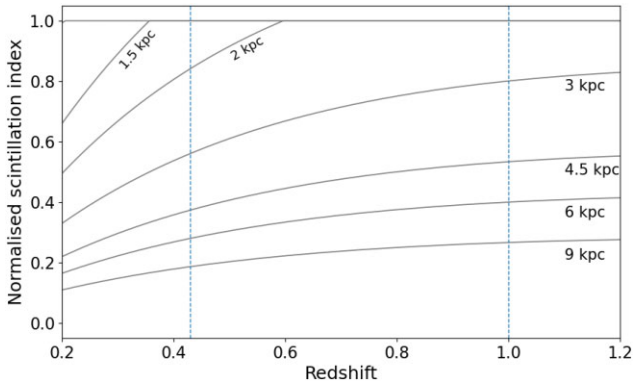

Figure 2. The predicted NSI for sources of different linear sizes as a function of redshift, similar to Chhetri et al. (2018). Vertical lines indicate the redshift range considered in this study. The plotted values assume an observing frequency of 150 MHz and an effective scattering distance $D = 1$ AU.

exclude them in the detection fraction estimate. Among the remaining 57 sources, the shallowest optical depth upper limit is < 9.08 km s^{-1}, which means that the spectrum has an optical depth sensitivity of 0.09 per 100 km s^{-1} channel. We consider only those detections that have an integrated optical depth > 9.08 km s^{-1} in our estimates. In our sample, only one detection (towards MRC 0531–237) has an integrated optical depth higher than this limit; one detection among 57 sources implies a detection fraction of 1.8 per cent$^{+4.0\ \text{per cent}}_{-1.5\ \text{per cent}}$. The uncertainties here and elsewhere in the paper correspond to 1σ, which are estimated using small-number Poisson statistics (Gehrels 1986).

We compile a sample of all sources at redshifts $0 < z < 0.42$, $0.42 < z < 1.00$, and $z > 1.00$, from the literature that have a sensitivity same or better than the above.[2] Here, for optical depth sensitivities which are reported for velocity resolutions smaller than 100 km s^{-1}, the upper limits on optical depth limits are divided by a factor of $\sqrt{100.0/v_{rep}}$, where v_{rep} is the reported velocity resolution. In the redshift range $0 < z < 0.42$ there are 54 detections and 378 non-detections (with upper limits) implying a detection fraction of 12.5 per cent$^{+1.9\ \text{per cent}}_{-1.7\ \text{per cent}}$ (see Fig. 6). In the range $0.42 < z < 1.00$, there are 7 detections and 283 non-detections, yielding a detection fraction of 2.4 per cent$^{+1.3\ \text{per cent}}_{-0.9\ \text{per cent}}$. Finally, at redshifts $z > 1.00$ there are 3 detections and 213 non-detections, implying a detection fraction of 1.4 per cent$^{+1.4\ \text{per cent}}_{-0.8\ \text{per cent}}$.

The detection fraction in our sample is consistent (within 1σ) with that in the literature sources at $0.42 < z < 1.0$. In Fig. 6, a significant decline between the detection fractions of sample at $z < 0.42$, and the samples at $0.42 < z < 1.00$ and $z > 1.0$ can be seen, although a difference in the detection fractions between $0.42 < z < 1.0$ and $z > 1.0$ intervals is not clear. Similar trends were reported earlier by various studies by Curran et al. (2008, 2013a) and Aditya & Kanekar (2018b). Also, recent FLASH pilot observations towards the Galaxy And Mass Assembly (GAMA) survey fields (e.g. Liske et al. 2015), reported by Su et al. (2022), have yielded a detection fraction of just 2.9 per cent$^{+9.7\ \text{per cent}}_{-2.6\ \text{per cent}}$.

The detectability of AGN associated H I 21-cm could depend on multiple factors, namely, the AGN UV and radio luminosities, the gas spin temperature, dust and cold gas content, and the gas covering factor. In the following sections, we will examine the effects of these factors in our sample.

6.2 *WISE* colours

The mid- to far-infrared spectral energy distribution (i.e. 6–100 μm SED) of dust-obscured AGNs is known to rise steeply with wavelength, when compared to unobscured sources (Mullaney et al. 2011). This is mainly due to the excess mid-infrared emission at longer wavelengths arising from the heated dust present along the line-of-sight. The *WISE* observes at 3.4 μm (W1), 4.6 μm (W2), 12.0 μm (W3), 24.0 μm (W4) wavelengths (Wright et al. 2010), and is particularly sensitive to the infrared luminous, dust-obscured galaxies. The obscured AGNs will have redder *WISE* W2-W3 mag colour, compared to unobscured ones. Based on this, Wright et al. (2010) have classified various galaxies using the *WISE* colours, as shown in Fig. 7.

We cross-matched the source co-ordinates with AllWISE catalogue Cutri et al. (2013), again using the TOPCAT application. Out of 62 sources, 33 sources have detections ($SNR \geq 5$) in W1, W2 & W3 bands, 27 have detections in only W1 & W2 bands, while 2 have detections in only W1 band. We have plotted the *WISE* W2-W3 mag and W1-W2 mag colours for the 60 sources with detections in W1 & W2 bands (and upper limit in W3 band) in Fig. 7. Here, the red markers represent quasars while the blue markers represent galaxies, as classified in the Tables 3 and 4, and the solid square markers represent detections of associated H I 21-cm absorption. The sources appear to be majorly distributed in the regions of QSOs, spirals, seyferts, starburts and LIRGs, and overall there is no significant clustering of the sources around any of the background classifications. Only one source (MRC 2232–232) is lying in the region of ULIRGs/obscured AGN. Further, Hickox et al. (2017) used a cut-off colour of W2 − W3 > 3.3 mag to segregate obscured sources from unobscured ones; the vertical dashed line in Fig. 7 represents this cut-off. In the Fig. 7 only 9 out of 33 sources with measurements of W2-W3 colour have W2-W3 > 3.3 mag, and, 13 out of 27 sources with upper limits on W2-W3 colour have limits higher than W2-W3 = 3.3 mag (i.e. lying on the right side of the vertical dashed line). It is interesting to note that among the three detections of H I 21-cm absorption in our sample, only one target, MRC 2216–281 at $z = 0.657$, has a W2-W3 colour of 3.5 mag, marginally higher than the cut-off of 3.3 mag, while the remaining two targets (MRC 2156–245 at $z = 0.862$ and MRC 0531–237 at $z = 0.851$) have W2 − W3 < 3.3 mag and do not show any strong signature for dust-obscuration (e.g. Wright et al. 2010; Hickox et al. 2017). This indicates that associated H I 21-cm absorption could have little relation to the presence of dust in the line of sight, in our sample. It is interesting to note that Glowacki et al. (2019) found null detections in their sample with W2 − W3 > 3.5 mag. However, their H I sensitivities were significantly poorer than the current survey; just six ASKAP antennas were used the observations. Curran et al. (2019) found a strong correlation between H I 21-cm absorption strength and V-K mag colour which indicates dust-reddening. Also, we note that

[2]The references for the data are: de Waard, Strom & Miley (1985); Mirabel (1989); Uson, Bagri & Cornwell (1991); De Breuck et al. (2003); Ishwara-Chandra, Dwarakanath & Anantharamaiah (2003); Vermeulen et al. (2003); Curran et al. (2006); Gupta et al. (2006); Carilli et al. (2007); Curran et al. (2008); Chandola, Saikia & Gupta (2010); Emonts et al. (2010); Salter et al. (2010); Chandola, Sirothia & Saikia (2011); Curran et al. (2011a, b); Allison et al. (2012); Chandola et al. (2012); Chandola, Gupta & Saikia (2013); Curran et al. (2013a, b); Srianand et al. (2015); Aditya, Kanekar & Kurapati (2016); Yan et al. (2016); Curran et al. (2016a, b); Aditya et al. (2017); Curran et al. (2017); Glowacki et al. (2017); Maccagni et al. (2017); Moss et al. (2017); Ostorero et al. (2017); Dutta, Srianand & Gupta (2018); Aditya & Kanekar (2018a, b); Aditya (2019); Grasha et al. (2019); Chowdhury, Kanekar & Chengalur (2020); Mhaskey et al. (2020); Aditya et al. (2021); Murthy et al. (2021, 2022); Su et al. (2022).

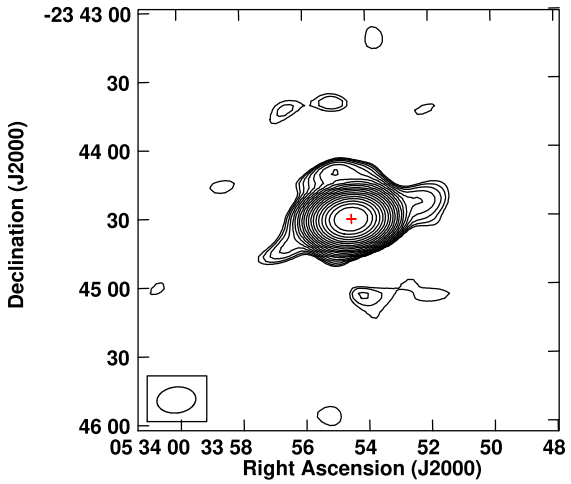

(a) The ASKAP continuum image at 856 MHz. The contours are at 1.05 mJy × (1, $\sqrt{2}$, 2, $2\sqrt{2}$, 4, $4\sqrt{2}$, 8, $8\sqrt{2}$, 16, $16\sqrt{2}$, 32, $32\sqrt{2}$, 64, $64\sqrt{2}$, 128, $128\sqrt{2}$, 256).

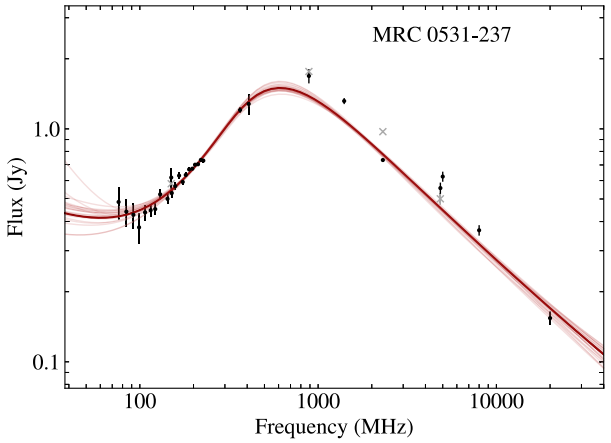

(b) SED fit for the radio flux densities of MRC 0531-237.

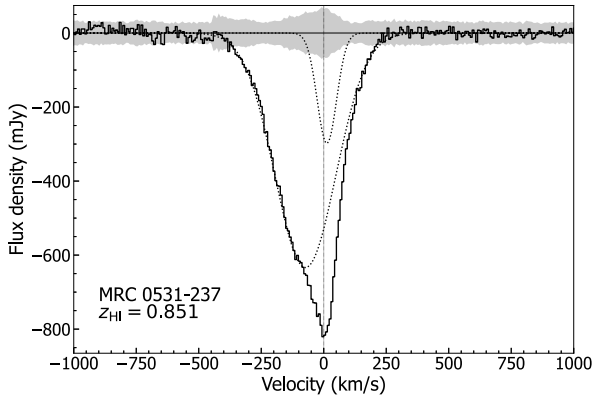

(c) The H I 21-cm absorption spectrum. The dotted lines are Gaussian fits to the absorption. The vertical line represents the AGN redshift, $z = 0.851$. And, the grey shaded region represents 5σ noise level. The higher noise level in channels sowing absorption is due to presence of low-level instrumental data corruption.

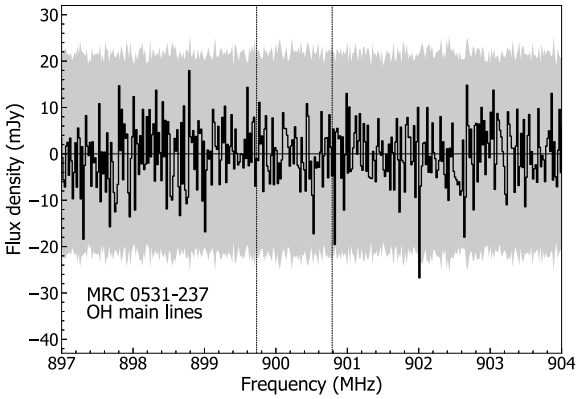

(d) OH spectrum towards MRC 0531-237. The vertical dashed lines represent the redshifted frequencies (w.r.t. $z = 0.851$) of OH main lines at 1665.402 MHz and 1667.359 MHz, respectively. The grey shaded region represents 5σ noise level.

Figure 3. ASKAP radio continuum, radio SED, and H I 21-cm absorption spectrum of MRC 0531–237.

Carilli et al. (1998) found four detections in a sample of five, where all the sources have W2 − W3 < 3.5 mag. Overall, given the small sample sizes, a further investigation using a larger sample would be needed to investigate the relation between H I 21-cm absorption and the *WISE* colours. Finally, a single source in our sample, MRC 2313–277, has a very low W2-W3 colour; MRC 2313–277 has a flat near-infrared spectrum, with W1 and W2 ≈12 mag, and may be representing a dust-poor elliptical galaxy.

6.3 Radio properties

Earlier studies at $z < 0.4$ have consistently reported a lower detection fraction of H I 21-cm absorption in extended radio sources ($\approx 10 - 15$ per cent) compared to compact sources with linear sizes smaller than a few kpc (≈ 30 per cent; GPS and CSS sources; see e.g. Gupta et al. 2006; Maccagni et al. 2017; Murthy et al. 2021). We note that earlier ASKAP searches towards GPS/CSS sources at $z < 0.1$, conducted by Allison et al. (2012) and Glowacki et al. (2017), yielded 7 detections in a sample of 66 sources (11 per cent$^{+6\ \text{per cent}}_{-4\ \text{per cent}}$). However, these observations had relatively very low spectral-sensitivity, where just 6 ASKAP antennas (now 36) were used. In the case of extended radio sources, the foreground absorbing gas, which is expected to be concentrated in the nuclear regions, could be only partially covering the background radio source. This will yield a low covering factor (see Curran et al. 2013c), causing a low apparent H I optical depth and detection fraction. In addition to a low covering factor, the expanding jets could ionize and expel the ambient gas away from the jet axis. In such a scenario, while the nuclear regions in larger sources would be cleared of gas and dust, young and compact sources would still be embedded in a dense medium (see more discussion in Section 6.6).

At higher redshifts, a redshift evolution in the gas properties and effects due to high AGN luminosities are also expected to become prominent, leading to a further reduction in the H I absorption

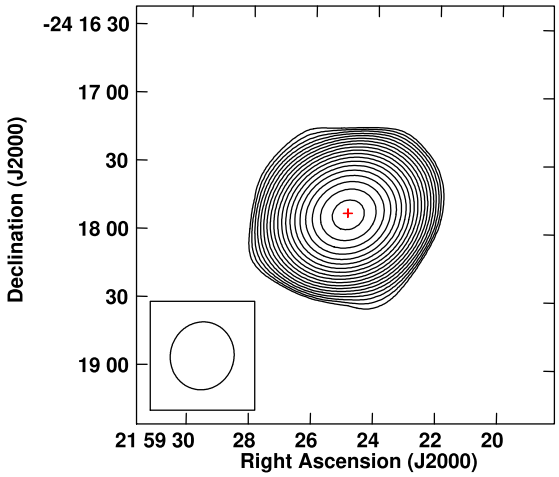

(a) The ASKAP continuum image at 856 MHz. The contours are at 0.95 mJy × (1, $\sqrt{2}$, 2, $2\sqrt{2}$, 4, $4\sqrt{2}$, 8, $8\sqrt{2}$, 16, $16\sqrt{2}$, 32, $32\sqrt{2}$, 64, $64\sqrt{2}$, 128, $128\sqrt{2}$, 256).

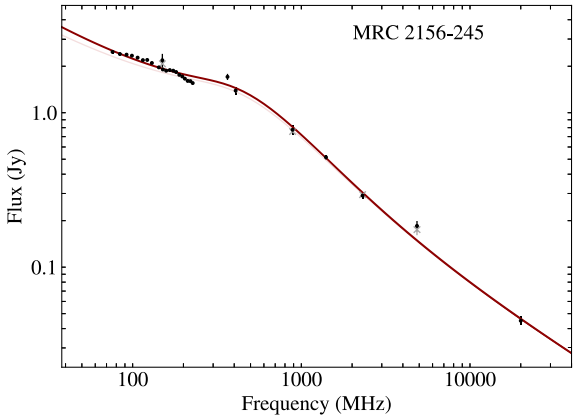

(b) SED fit for the radio flux densities of MRC 2156-245.

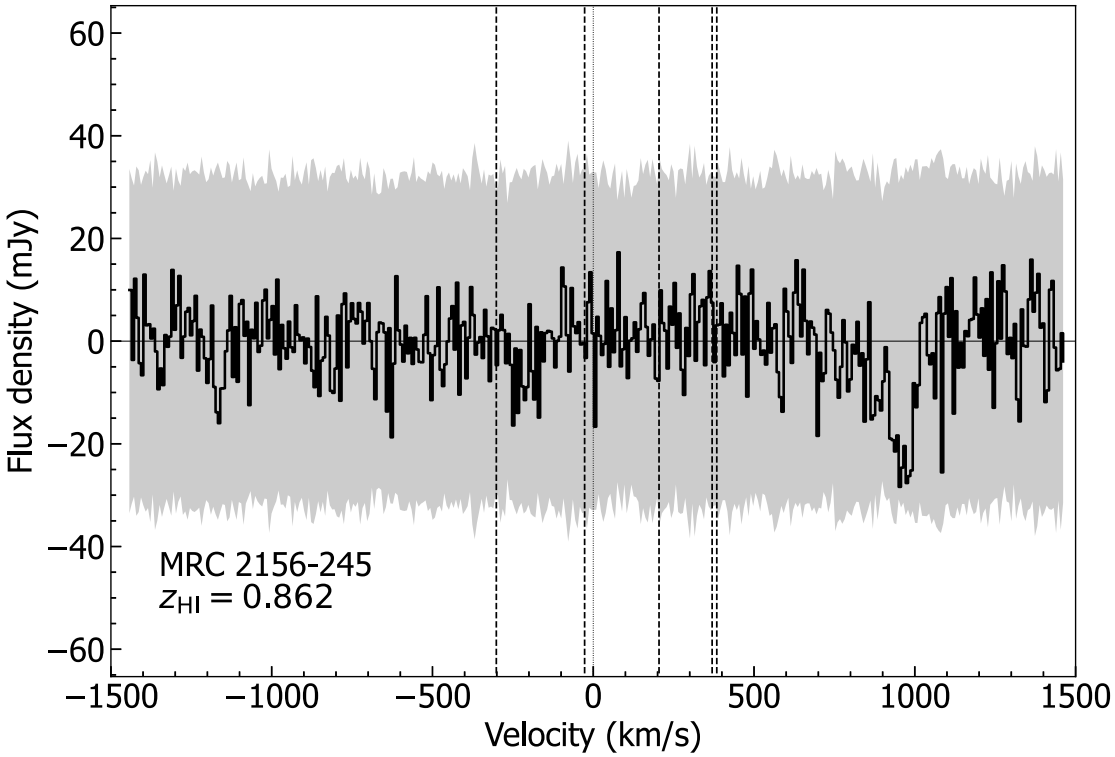

(c) The H I 21-cm absorption spectrum. The vertical dashed lines represent, from left to right, the positions of [Ne V], Hβ, Mg II, [O II] and Hγ respectively. The vertical dotted line at 0 km s^{-1} represents the reference for the average redshift, z = 0.862. The absorption feature can be seen near the velocity of $\approx$ 1000 km s^{-1}.

Figure 4. ASKAP radio continuum, radio SED, and H I 21-cm absorption spectrum of MRC 2156–245.

strength and detection fraction (e.g. Curran et al. 2008; Aditya & Kanekar 2018b). However, as noted in Section 1, at $z > 1$, the available individual searches are small in sample size, and are mostly targeted for compact sources. While at lower redshifts, the searches are heterogeneous with a mixture of extended and compact sources, which inhibits rigorous testing of various scenarios.

In our sample, there are four peaked-spectrum sources and nine compact steep-spectrum sources (see Table 6). Two sources with detections of H I 21-cm absorption are classified as peaked-spectrum sources (MRC 0531–237 and MRC 2216–281), while the remaining one is classified as a CSS source (MRC 2156–245). Overall, the detection fraction among peaked-spectrum and CSS class sources is 23 per cent$^{+22\ \text{per cent}}_{-13\ \text{per cent}}$ (3 out of 13). For comparison, Vermeulen et al. (2003) detected 8 absorbers in a sample of 19 GPS and CSS sources at redshifts $0.42 < z < 0.84$ (similar to our range), yielding a detection fraction of 42.1 per cent$^{+20.8\ \text{per cent}}_{-14.6\ \text{per cent}}$ (see Fig. 6). Albeit with large

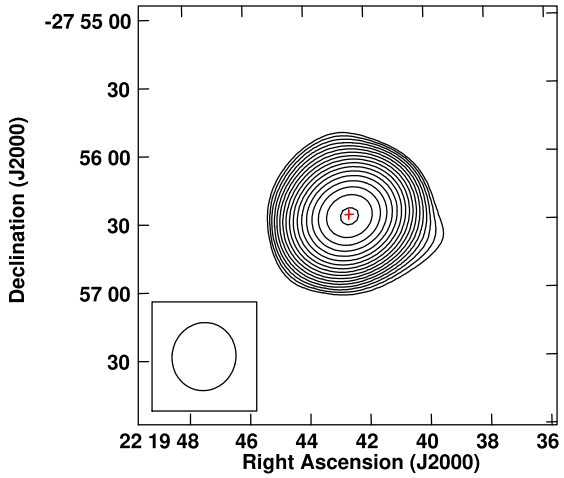

(a) The ASKAP continuum image at 856 MHz. The contours are at 5.7 mJy × (1, $\sqrt{2}$, 2, $2\sqrt{2}$, 4, $4\sqrt{2}$, 8, $8\sqrt{2}$, 16, $16\sqrt{2}$, 32, $32\sqrt{2}$, 64, $64\sqrt{2}$, 128, $128\sqrt{2}$, 256).

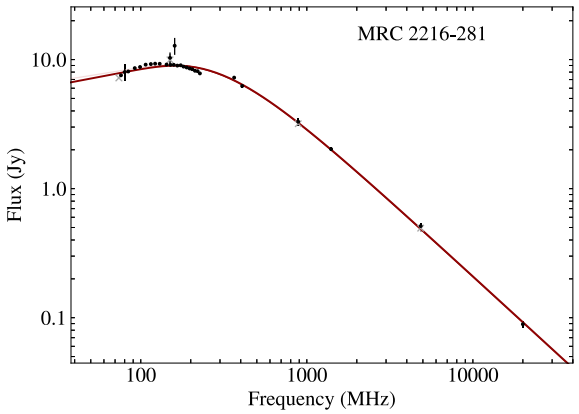

(b) SED fit for the radio flux densities of MRC 2216-281.

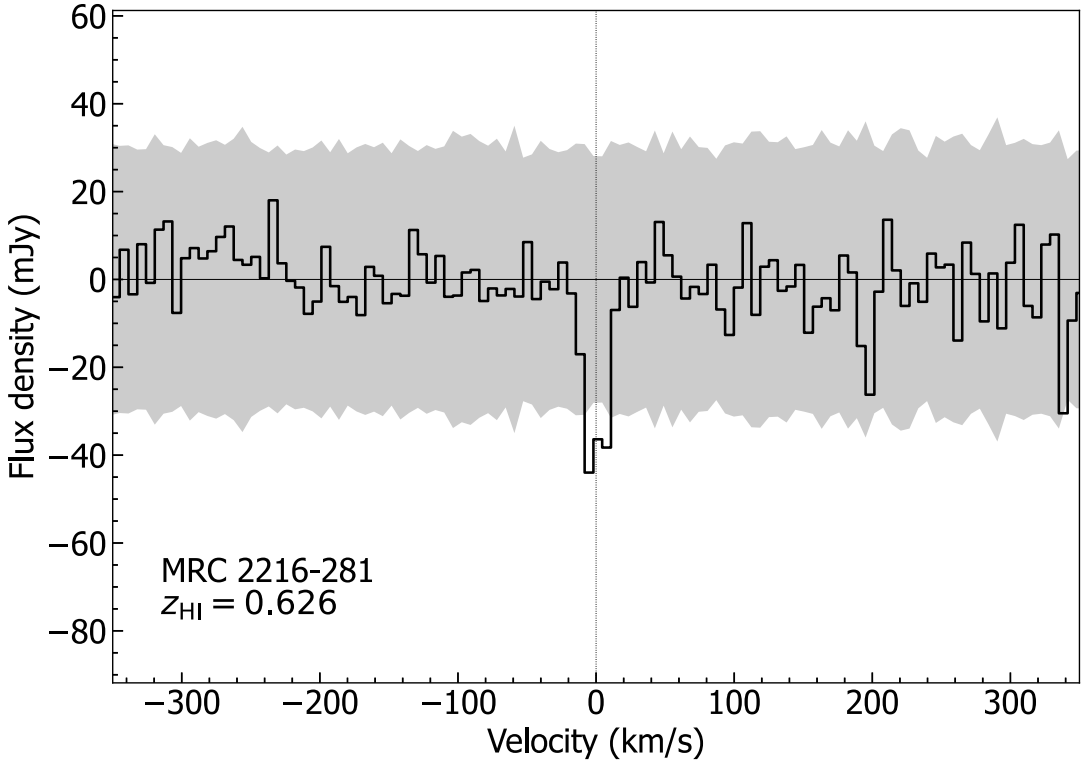

(c) The H I 21-cm absorption spectrum. The velocities are relative to $z = 0.626$. To note: the AGN redshift reported in the literature is $z = 0.657 \pm 0.050$ (McCarthy et al. 1996)

Figure 5. ASKAP radio continuum, radio SED, and H I 21-cm absorption spectrum of MRC 2216–281.

uncertainties, our estimates are consistent with those of Vermeulen et al. (2003) within 1σ. We find no detection in the remaining 48 targets, implying a detection fraction of 0 per cent$^{+4 \text{ per cent}}$. The preponderance of such sources in our sample, which have an extended radio morphology, would partially explain the overall low detection fraction in our sample (as discussed above), although the effects of a redshift evolution in gas properties and the AGN luminosity, would still need to be investigated.

6.4 H I absorption in sources with interplanetary scintillation

The two targets MRC 2156–245, at $z = 0.862$, and MRC 2216–281, at $z = 0.657$, that have been detected with associated H I 21-cm absorption, are among the ones with the highest NSI in the sample, 0.79 and 0.82 (see Table 5), respectively. For the remaining sample the median detected NSI is 0.36. While the ASKAP observations have a spatial resolution of ≈15 arcsec, which cannot reveal sub-arcsec structure, the high NSI for the two radio sources with associated

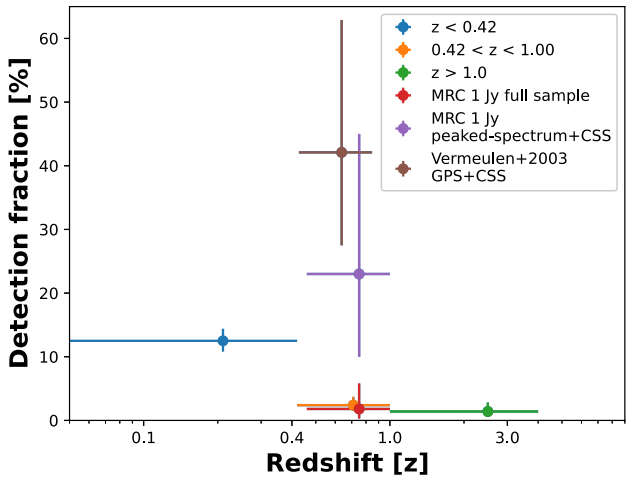

Figure 6. The detection fraction of associated H I 21-cm absorbers in the literature, at various redshift intervals. The detections fractions for various markers are: $12.5^{+1.9}_{-1.7}$per cent (Blue), $2.4^{+1.3}_{-0.9}$per cent (Orange), $1.4^{+1.4}_{-0.8}$per cent (Green), $1.8^{+4.0}_{-1.5}$per cent (Red), $23.0^{+22.1}_{-13.3}$per cent (Violet) and $42.1^{20.8}_{14.6}$per cent (Brown).

H I 21-cm absorption indicates a compact sub-arcsec structure, or, presence of compact components.

The detection of H I 21-cm absorption reiterates the radio source compactness, and demonstrates the effectiveness of the IPS technique, because the neutral gas covering factor is expected to be higher (≈1 see e.g. Curran et al. 2013c) for compact sources, yielding high apparent optical depth and detection chances of H I 21-cm absorption. Indeed, the detection fraction of associated H I 21-cm absorption is known to be higher in low-redshift gigahertz peaked-spectrum (GPS) and compact steep-spectrum (CSS) sources compared to extended radio sources (e.g. Pihlström, Conway & Vermeulen 2003; Gupta et al. 2006; Maccagni et al. 2017). Given the complexities involved in conducting VLBI surveys, like the calibration and slow survey rate, the IPS technique could be an efficient alternative to identify compact radio sources, and precursors for H I 21-cm absorption surveys. We also emphasize the need to further test the high H I 21-cm detection fraction in sources with high NSI.

6.5 AGN UV and radio luminosities

Here, we examine the effect of radio and UV luminosities of the AGN on the detections of H I 21-cm absorption in our sample (Table 7) . We plot the rest-frame 1.4 GHz radio luminosity (L_{rad}) for all our targets in the left panel of Fig. 8. A gradual increase in the source luminosities as a function of redshift can be seen, which is due to a Malmquist selection bias (in a brightness-limited survey) where the high-redshift sources would have higher intrinsic luminosities. The radio luminosities span over $25.4 - 27.7$ W Hz^{-1}. We note that the two sources with detection of H I 21-cm absorption, MRC 0531–237 and MRC 2216–281, have the highest radio luminosities, and the third detection, MRC 2156–245, has $L_{rad} > 27$ W Hz^{-1} which is higher than a majority of the sources in the sample (see left panel of Fig. 8). This indicates that the 1.4 GHz radio luminosity is likely less effective in raising the gas spin temperature, and thereby, reducing the H I absorption strength. And thus, it is probably not a dominant factor for the low detection rate in our sample.

In the upper-right and the lower-right panels of Fig. 8, we plot the ultraviolet ionizing photon rate (Q; in s^{-1}), and 1216 Å UV luminosity (L_{UV}; in W Hz^{-1}) respectively, for 26 targets of our sample. For the remaining sources there were not enough optical or UV photometric data points available in the literature, either to estimate the 1216 Å luminosity (and ionizing photon rate) or to estimate an upper limit for the same. We note that among the 26 targets, 12 have only upper limits for the 1216 Å luminosity and photon rates. Unfortunately, the three detections of H I 21-cm absorption in our sample do not have enough literature data, and are thus not plotted in these figures. While it is difficult to draw conclusions from the limited data, we note that among the 26 sources a majority (18) have $Q < 10^{56}$ s^{-1} and $L_{UV} < 10^{23}$ W Hz^{-1}. These limits represent approximate cut-offs of UV photon rate and luminosity at 1216 Å, proposed by Curran et al. (2008, 2019), above which all the neutral gas in the AGN surroundings is expected to be completely ionized. Assuming a similar distribution of luminosities and ionizing photon rates for the full sample of 62, only 19 sources would have 1216 Å luminosity and photon rate higher than the cut-offs, while the remaining 43 sources would have lower values, suggesting that the 1216 Å radiation from the AGN may not effectively ionize all the neutral gas in the AGN surroundings for a majority of the sources in our sample. However, we strongly note that this effect needs to be further investigated using a larger, statistically significant sample.

6.6 Dust and C IV properties

Metal absorption lines associated with quasars provide valuable information about the nuclear environments, probing the gas along various sight-lines towards the quasar. Baker et al. (2002) studied the C IV 1548 Å and 1550 Å absorption and emission lines associated with the quasars in the MRC sample. Eight sources from the current sample (including MRC 2156–245, detected with H I 21-cm absorption) are a part of this study. While both C IV 1550 Å emission and 1548 Å absorption were detected towards six of these sources, only emission was detected towards one source, and, MRC 2156–245 was too faint in the b_J band (20.2 mag; see Baker et al. 2002) to extract an optical spectrum. However, MRC 2156–245 has a very red optical spectral index, $\alpha_{opt} = 2$, measured between 3500 Å and 10 000 Å, which is the second highest in the sample of Baker et al. (2002). Both the faintness and red spectral properties indicate presence of significant amount of dust along the line of sight. We estimate a gas-to-dust ratio, N_{HI} E(B − V), of 5.6×10^{21} cm^{-2} mag^{-1} (see Baker et al. 2002; Neeleman et al. 2016, for B and V magnitudes), which is close to the mean Galactic ratio of 5.2×10^{21} cm^{-2} mag^{-1} (Shull & van Steenberg 1985), again implying high dust content (see also Curran et al. 2019). However, we note here that the N_{HI} is estimated using the H I 21-cm absorption line which probes only the cold component of the gas, while the total H I column density could be larger than this. In passing, on contrary, we note that the *WISE* colours for the source does not indicate any strong signature for dust-obscuration, as discussed in Section 6.2 above.

As previously discussed in Section 6.3, earlier studies reported a relatively high detection fraction of H I 21-cm absorption towards compact radio sources, which is also seen in this work. A high detection fraction of H I 21-cm absorption among compact radio sources is interpreted as the result of a high gas covering factor against the background radio source, yielding a high apparent optical depth (e.g. Pihlström, Conway & Vermeulen 2003; Curran et al. 2013c), whereas, the covering factor would be low in the case of extended radio sources. However, it is currently not clear from these studies whether the apparently high absorption strength in compact radio sources is solely due to a high gas covering factor, or, if these systems indeed harbour higher gas densities.

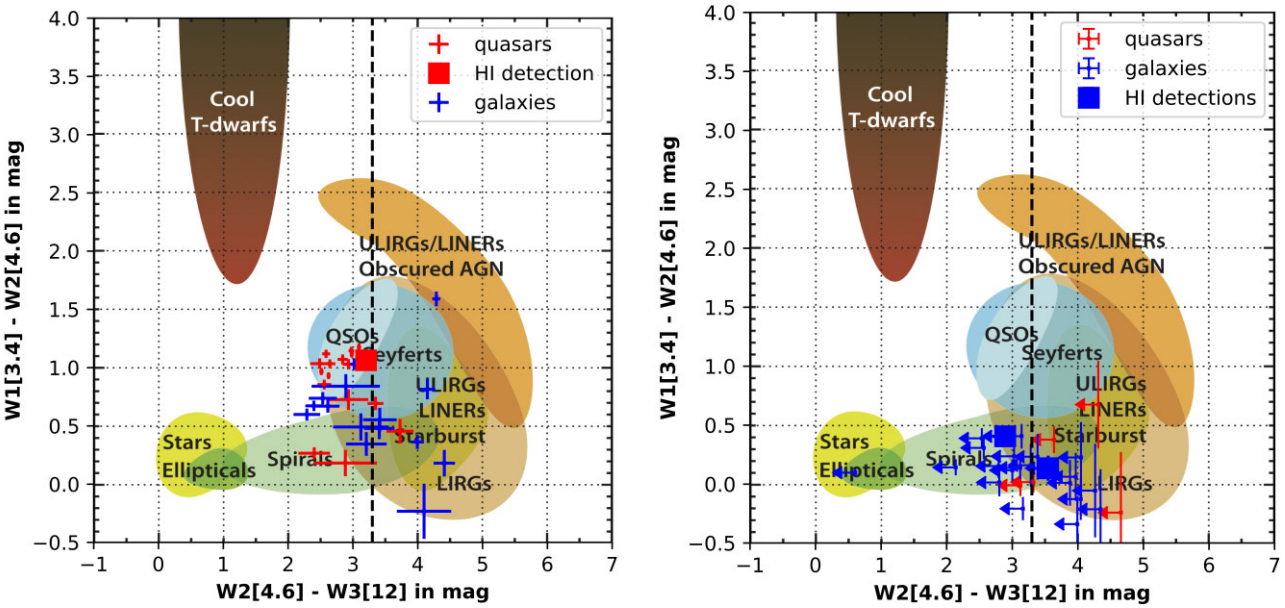

Figure 7. *WISE* colour–colour plot for 60 sources in our sample, plotted over the source classification obtained from Wright et al. (2010). For two sources, MRC 0430–235 & MRC 2348–235 the emission is detected only in W1 band. The left panel shows the *WISE* colours for 33 sources which are detected in W1, W2, and W3 bands. The panel at right shows 27 sources that are detected in only W1 & W2 bands, and have an upper limit for the W2-W3 mag. The vertical dashed line at W2-W3 = 3.3 mag represents the cut-off reported by Hickox et al. (2017) to segregate dust-obscured sources.

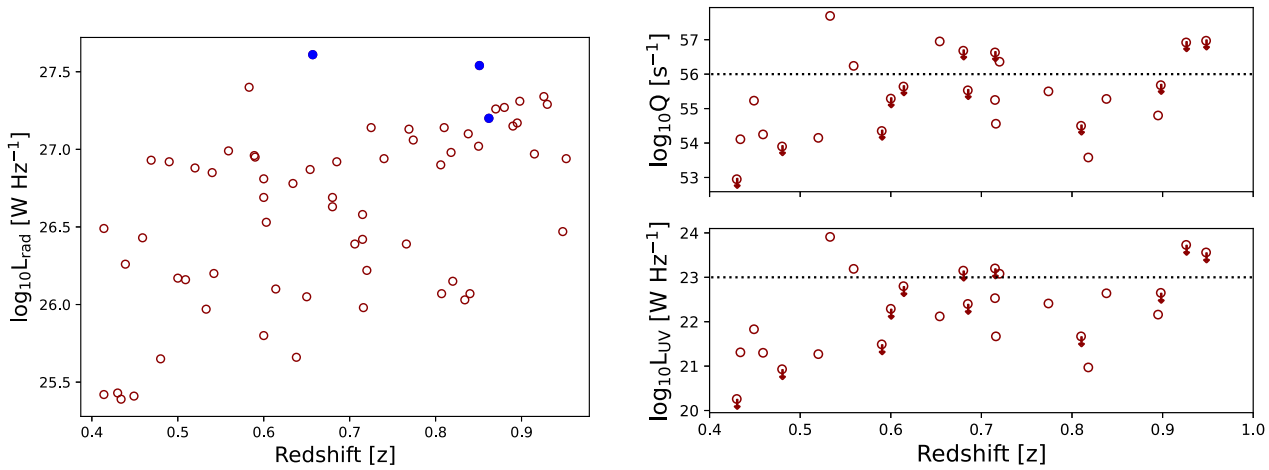

Figure 8. Left panel: Rest-frame 1.4 GHz radio luminosity as a function of redshift for all 62 targets. The solid blue markers represent detections of H I 21-cm absorption, while the hollow red markers represent non detections. Upper right panel: the ionizing photon rate as a function of redshift. Bottom right panel: ultraviolet luminosity, at 1216 Å, as a function of redshift. In both these panels the red hollow markers represent non-detections of H I 21-cm absorption for 26 targets with available data. Among these, 14 are measurements (of ionizing photon rate and UV luminosity), while remaining 12 are upper limits represented by 'down' arrows. We particularly note that the three detections of H I 21-cm absorption do not have UV data. The horizontal dotted lines represent the cut-offs suggested by Curran et al. (2008, 2019). However, we note that the cut-offs are to be treated as approximate limits. Complete ionization would result in cases of significant departure of the luminosity from these limits.

Baker et al. (2002) find a correlation between the C IV equivalent width and the optical spectral index, $\alpha_{\rm opt}$, for the sample of MRC quasars in their study. The authors argue that a high optical spectral index is an indication of presence of dust, and the absorbing clouds comprise of both dust and highly ionized gas. They also find a strong inverse correlation between the C IV 1548 Å absorption strength and the projected linear size of the radio sources; CSS and GPS sources, with sizes $\lesssim$ few $\times$ kpc, show the strongest absorption. Stronger absorption against the cores of compact radio sources indicate that the immediate surroundings of young radio sources could be hosting excess dust and gas, when compared to extended radio sources. Compact sources are believed to be the 'younger' or undeveloped stages of an AGN (e.g. O'Dea, Baum & Stanghellini 1991; O'Dea 1998), when they are engulfed in a cocoon of gas and dust. As the jets expand, the ambient dust would either be destroyed or pushed away from the jet axis, over a time-scale of $\sim 10^{4-6}$ yr (e.g. De Young 1998). Strong absorption lines could hence arise in the opportune stages of the AGN when the lobes are still embedded in the cocoon. The high H I 21-cm detection fraction in GPS and CSS sources could then be a result of both high gas covering factor and neutral gas density.

7 SUMMARY

We report a pilot search for associated H I 21-cm absorption towards bright radio sources from the MRC/1 Jy sample. Our work uses pilot survey data from FLASH covering intermediate redshifts ($0.42 < z < 1.00$). We achieved a median 3σ upper limit on integrated optical depth of 2.07 km s^{-1}, for our sample of 62 MRC sources. We discover three new associated H I 21-cm absorbers from the search; towards MRC 0531–237 at $z = 0.851$, MRC 2156–245 at $z = 0.862$, and MRC 2216–281 at $z = 0.626$. The overall detection fraction is $5\,\mathrm{per\,cent}^{+5\,\mathrm{per\,cent}}_{-3\,\mathrm{per\,cent}}$, which is relatively low compared to the detection fraction at low redshifts ($z < 0.4$), reported in earlier studies. The absorber towards MRC 0531–237 has the strongest H I 21-cm optical depth (143.80 ± 0.35 km s^{-1}) so far reported. We find that the continuum sources of all the three detections are intrinsically compact, showing either an inverted SEDs and/or high NSI. We do not find any significant relation between the H I 21-cm absorption and dust obscuration as inferred from the *WISE* colours. Also, we do not find that a high 1.4 GHz radio luminosities of the sources has a significant effect on H I 21-cm absorption strength and detection fraction. The preponderance of extended radio sources in our sample could be a dominant cause for an overall low detection fraction in our sample, although the effects of high UV luminosities of AGNs and a redshift evolution in gas properties would still need to be investigated using a larger sample.

ACKNOWLEDGEMENTS

This scientific work uses data obtained from Inyarrimanha Ilgari Bundara/the Murchison Radio-astronomy Observatory. We acknowledge the Wajarri Yamaji People as the Traditional Owners and native title holders of the Observatory site. CSIRO's ASKAP radio telescope is part of the Australia Telescope National Facility (https://ror.org/05qajvd42). Operation of ASKAP is funded by the Australian Government with support from the National Collaborative Research Infrastructure Strategy. ASKAP uses the resources of the Pawsey Supercomputing Research Centre. Establishment of ASKAP, Inyarrimanha Ilgari Bundara, the CSIRO Murchison Radio-astronomy Observatory, and the Pawsey Supercomputing Research Centre are initiatives of the Australian Government, with support from the Government of Western Australia and the Science and Industry Endowment Fund. This research was supported by the Australian Research Council Centre of Excellence for All Sky Astrophysics in 3 Dimensions (ASTRO 3D), through project number CE170100013. Support for the operation of the MWA is provided by the Australian Government (NCRIS), under a contract to Curtin University administered by Astronomy Australia Limited. This research has made use of the NASA/IPAC Extragalactic Database (NED), which is funded by the National Aeronautics and Space Administration and operated by the California Institute of Technology. MG acknowledges support from IDIA and was partially supported by the Australian Government through the Australian Research Council's Discovery Projects funding scheme (DP210102103). TA acknowledges financial support from Pinghu Laboratory.

DATA AVAILABILITY

All data from FLASH Pilot 1 and 2 observations are available online at the CSIRO ASKAP Science Data Archive (CASDA; https://research.csiro.au/casda/), with the project code AS109.

REFERENCES

Aditya J. N. H. S., 2019, MNRAS, 482, 5597
Aditya J. N. H. S., Kanekar N., 2018a, MNRAS, 473, 59
Aditya J. N. H. S., Kanekar N., 2018b, MNRAS, 481, 1578
Aditya J. N. H. S., Kanekar N., Kurapati S., 2016, MNRAS, 455, 4000
Aditya J. N. H. S., Kanekar N., Prochaska J. X., Day B., Lynam P., Cruz J., 2017, MNRAS, 465, 5011
Aditya J. N. H. S., Jorgenson R., Joshi V., Singh V., An T., Chandola Y., 2021, MNRAS, 500, 998
Allison J. R. et al., 2012, MNRAS, 423, 2601
Allison J. R. et al., 2015, MNRAS, 453, 1249
Allison J. R. et al., 2017, MNRAS, 465, 4450
Allison J. R. et al., 2022, Publ. Astron. Soc. Austr., 39, e010
Araya E. D., Rodríguez C., Pihlström Y., Taylor G. B., Tremblay S., Vermeulen R. C., 2010, AJ, 139, 17
Baker J. C., Hunstead R. W., Kapahi V. K., Subrahmanya C. R., 1999, ApJS, 122, 29
Baker J. C., Hunstead R. W., Athreya R. M., Barthel P. D., de Silva E., Lehnert M. D., Saunders R. D. E., 2002, ApJ, 568, 592
Becker R. H., White R. L., Helfand D. J., 1995, ApJ, 450, 559
Bird S., Garnett R., Ho S., 2017, MNRAS, 466, 2111
Boller T., Freyberg M. J., Trümper J., Haberl F., Voges W., Nandra K., 2016, A&A, 588, A103
Braun R., 2012, ApJ, 749, 87
Brown M. J. I., Webster R. L., Boyle B. J., 2001, AJ, 121, 2381
Callingham J. R. et al., 2017, ApJ, 836, 174
Cantalupo S., Porciani C., Lilly S. J., Miniati F., 2005, ApJ, 628, 61
Carilli C. L., Menten K. M., Reid M. J., Rupen M. P., Yun M. S., 1998, ApJ, 494, 175
Carilli C. L., Wang R., van Hoven M. B., Dwarakanath K., Chengalur J. N., Wyithe S., 2007, AJ, 133, 2841
Chakraborty A., Roy N., 2023, MNRAS, 519, 4074
Chandola Y., Saikia D. J., Gupta N., 2010, MNRAS, 403, 269
Chandola Y., Sirothia S. K., Saikia D. J., 2011, MNRAS, 418, 1787
Chandola Y., Sirothia S. K., Saikia D. J., Gupta N., 2012, Bull. Astron. Soc. India, 40, 139
Chandola Y., Gupta N., Saikia D. J., 2013, MNRAS, 429, 2380
Chhetri R., Morgan J., Ekers R. D., Macquart J. P., Sadler E. M., Giroletti M., Callingham J. R., Tingay S. J., 2018, MNRAS, 474, 4937
Chowdhury A., Kanekar N., Chengalur J. N., 2020, ApJ, 900, L30
Clarke M., 1964, Ph.D. thesis; Cambridge University
Condon J. J., Cotton W. D., Greisen E. W., Yin Q. F., Perley R. A., Taylor G. B., Broderick J. J., 1998, AJ, 115, 1693
Cseh D., Fuhl A., Frey S., 2008, in Proc. Sci., The 9th European VLBI Network Symposium on The role of VLBI in the Golden Age for Radio Astronomy and EVN Users Meeting (IX EVN Symposium). SISSA, Trieste, PoS#074
Curran S. J., Whiting M. T., 2010, ApJ, 712, 303
Curran S. J., Whiting M. T., Murphy M. T., Webb J. K., Longmore S. N., Pihlström Y. M., Athreya R., Blake C., 2006, MNRAS, 371, 431
Curran S. J., Whiting M. T., Wiklind T., Webb J. K., Murphy M. T., Purcell C. R., 2008, MNRAS, 391, 765
Curran S. J. et al., 2011a, MNRAS, 413, 1165
Curran S. J., Whiting M. T., Webb J. K., Athreya R., 2011b, MNRAS, 414, L26
Curran S. J., Whiting M. T., Sadler E. M., Bignell C., 2013a, MNRAS, 428, 2053
Curran S. J., Whiting M. T., Tanna A., Sadler E. M., Pracy M. B., Athreya R., 2013b, MNRAS, 429, 3402
Curran S. J., Allison J. R., Glowacki M., Whiting M. T., Sadler E. M., 2013c, MNRAS, 431, 3408
Curran S. J., Allison J. R., Whiting M. T., Sadler E. M., Combes F., Pracy M. B., Bignell C., Athreya R., 2016a, MNRAS, 457, 3666
Curran S. J., Duchesne S. W., Divoli A., Allison J. R., 2016b, MNRAS, 462, 4197
Curran S. J., Hunstead R. W., Johnston H. M., Whiting M. T., Sadler E. M., Allison J. R., Bignell C., 2017, MNRAS, 470, 4600

Curran S. J., Hunstead R. W., Johnston H. M., Whiting M. T., Sadler E. M., Allison J. R., Athreya R., 2019, MNRAS, 484, 1182
Cutri R. M. et al.,2013, 2MASS All Sky Catalog of Point Sources. Explanatory Supplement to the AllWISE Data Release Products
De Breuck C. et al., 2003, A&A, 401, 911
de Waard G. J., Strom R. G., Miley G. K., 1985, A&A, 145, 479
De Young D. S., 1998, ApJ, 507, 161
DeBoer D. R. et al., 2009, IEEE Proc., 97, 1507
Dickey J. M., Crovisier J., Kazes I., 1981, A&A, 98, 271
Douglas J. N., Bash F. N., Bozyan F. A., Torrence G. W., Wolfe C., 1996, AJ, 111, 1945
Draine B. T., 2011, Physics of the Interstellar and Intergalactic Medium. Princeton Univ. Press, Princeton
Dutta R., Srianand R., Gupta N., 2018, MNRAS, 480, 947
Dwelly T. et al., 2017, MNRAS, 469, 1065
Emonts B. H. C. et al., 2010, MNRAS, 406, 987
Evans I. N. et al., 2019, American Astronomical Society, HEAD meeting #17, id.114.01
Evans P. A. et al., 2020, ApJS, 247, 54
Falomo R., 1991, AJ, 102, 1991
Fernández X. et al., 2016, ApJ, 824, L1
Field G. B., 1959, ApJ, 129, 536
Gehrels N., 1986, ApJ, 303, 336
Glowacki M. et al., 2017, MNRAS, 467, 2766
Glowacki M. et al., 2019, MNRAS, 489, 4926
Grasha K., Darling J., Bolatto A., Leroy A. K., Stocke J. T., 2019, ApJS, 245, 3
Gupta N., Salter C. J., Saikia D. J., Ghosh T., Jeyakumar S., 2006, MNRAS, 373, 972
Gupta N., Momjian E., Srianand R., Petitjean P., Noterdaeme P., Gyanchandani D., Sharma R., Kulkarni S., 2018, ApJ, 860, L22
Gupta N. et al., 2021, ApJS, 255, 28
Healey S. E., Romani R. W., Taylor G. B., Sadler E. M., Ricci R., Murphy T., Ulvestad J. S., Winn J. N., 2007, ApJS, 171, 61
Hewish A., Scott P. F., Wills D., 1964, Nature, 203, 1214
Hickox R. C., Myers A. D., Greene J. E., Hainline K. N., Zakamska N. L., DiPompeo M. A., 2017, ApJ, 849, 53
Hotan A. W. et al., 2021, Publ. Astron. Soc. Austr., 38, e009
Intema H. T., Jagannathan P., Mooley K. P., Frail D. A., 2017, A&A, 598, A78
Ishwara-Chandra C. H., Dwarakanath K. S., Anantharamaiah K. R., 2003, J. Astrophys. Astron., 24, 37
Kanekar N., Briggs F. H., 2004, New Astron. Rev., 48, 1259
Kanekar N. et al., 2014, MNRAS, 438, 2131
Kapahi V. K., Athreya R. M., van Breugel W., McCarthy P. J., Subrahmanya C. R., 1998a, ApJS, 118, 275
Kapahi V. K., Athreya R. M., Subrahmanya C. R., Baker J. C., Hunstead R. W., McCarthy P. J., van Breugel W., 1998b, ApJS, 118, 327
Krumholz M. R., McKee C. F., Tumlinson J., 2009, ApJ, 699, 850
Large M. I., Mills B. Y., Little A. G., Crawford D. F., Sutton J. M., 1981, MNRAS, 194, 693
Liske J. et al., 2015, MNRAS, 452, 2087
Little L. T., Hewish A., 1966, MNRAS, 134, 221
Maccagni F. M., Morganti R., Oosterloo T. A., Geréb K., Maddox N., 2017, A&A, 604, A43
Mahony E. K. et al., 2022, MNRAS, 509, 1690
Maloney P. R., Hollenbach D. J., Tielens A. G. G. M., 1996, ApJ, 466, 561
Mauch T., Murphy T., Buttery H. J., Curran J., Hunstead R. W., Piestrzynski B., Robertson J. G., Sadler E. M., 2003, MNRAS, 342, 1117
McCarthy P. J., Kapahi V. K., van Breugel W., Persson S. E., Athreya R., Subrahmanya C. R., 1996, ApJS, 107, 19
McConnell D. et al., 2020, Publ. Astron. Soc. Austr., 37, e048
Mhaskey M., Paul S., Gupta N., Mukherjee D., Gopal-Krishna, 2020, A&A, 643, A174
Mirabel I. F., 1989, ApJ, 340, L13
Morgan J. S. et al., 2018, MNRAS, 473, 2965
Morganti R., Oosterloo T., 2018, A&AR, 26, 4
Morganti R., Fogasy J., Paragi Z., Oosterloo T., Orienti M., 2013, Science, 341, 1082
Moss V. A. et al., 2017, MNRAS, 471, 2952
Mullaney J. R., Alexander D. M., Goulding A. D., Hickox R. C., 2011, MNRAS, 414, 1082
Murthy S., Morganti R., Oosterloo T., Maccagni F. M., 2021, A&A, 654, A94
Murthy S., Morganti R., Kanekar N., Oosterloo T., 2022, A&A, 659, A185
Neeleman M., Prochaska J. X., Ribaudo J., Lehner N., Howk J. C., Rafelski M., Kanekar N., 2016, ApJ, 818, 113
Noterdaeme P., López S., Dumont V., Ledoux C., Molaro P., Petitjean P., 2012, A&A, 542, L33
O'Dea C. P., 1998, PASP, 110, 493
O'Dea C. P., Baum S. A., Stanghellini C., 1991, ApJ, 380, 66
Ostorero L., Morganti R., Diaferio A., Siemiginowska A., Stawarz Ł., Moderski R., Labiano A., 2017, ApJ, 849, 34
Pihlström Y. M., Conway J. E., Vermeulen R. C., 2003, A&A, 404, 871
Pocock A. S., Blades J. C., Penston M. V., Pettini M., 1984, MNRAS, 210, 373
Salter C. J., Saikia D. J., Minchin R., Ghosh T., Chandola Y., 2010, ApJ, 715, L117
Shull J. M., van Steenberg M. E., 1985, ApJ, 294, 599
Snellen I. A. G., Schilizzi R. T., de Bruyn A. G., Miley G. K., Rengelink R. B., Roettgering H. J., Bremer M. N., 1998, A&AS, 131, 435
Srianand R., Gupta N., Momjian E., Vivek M., 2015, MNRAS, 451, 917
Su R. et al., 2022, MNRAS, 516, 2947
Taylor M. B., 2005, in Shopbell P., Britton M., Ebert. R., eds, ASP Conf. Ser. Vol. 347, Astronomical Data Analysis Software and Systems XIV. Astron. Soc. Pac., San Francisco, p. 29
Uson J. M., Bagri D. S., Cornwell T. J., 1991, Phys. Rev. Lett., 67, 3328
Vermeulen R. C. et al., 2003, A&A, 404, 861
Wang J., Cen X., Xu J., Qian T., 1997, ApJ, 491, 501
Wayth R. B. et al., 2015, Publ. Astron. Soc. Austr., 32, e025
Webb N. A. et al., 2020, A&A, 641, A136
Whiting M. T., 2020, in Ballester P., Ibsen J., Solar M., Shortridge K., eds, ASP Conf. Ser. Vol. 522, Astronomical Data Analysis Software and Systems XXVII. Astron. Soc. Pac., San Francisco, p. 469
Wright E. L. et al., 2010, AJ, 140, 1868
Yan T., Stocke J. T., Darling J., Momjian E., Sharma S., Kanekar N., 2016, AJ, 151, 74

SUPPORTING INFORMATION

Supplementary data are available at *MNRAS* online.

supplementary_material.zip

Please note: Oxford University Press is not responsible for the content or functionality of any supporting materials supplied by the authors. Any queries (other than missing material) should be directed to the corresponding author for the article.

APPENDIX A: NOTES ON INDIVIDUAL SOURCES

MRC 0030–220

A 4.8 GHz continuum image from Kapahi et al. (1998b) shows that this $z = 0.806$ quasar has two lobes separated by about 4 arcsec. The central core is relatively weak (9.5 mJy at 8.4 GHz). MRC 0030-220 was observed with *HST* by Baker et al. (2002), who detected associated C IV absorption. The *HST* spectrum was re-analysed by Neeleman et al. (2016) to search for intervening Damped Lyman-α (DLA) absorption lines in the redshift range 0.533 to 0.788, but no Ly α absorption was seen.

MRC 0030–220 has been detected as an X-ray source by *Chandra*/ACIS (2CXO J003244.6–214420; Evans et al. 2019), with a rest-frame X-ray luminosity L(2–10 keV) of 6 ($\pm$2) $\times$ 10^{44} erg s^{-1}.

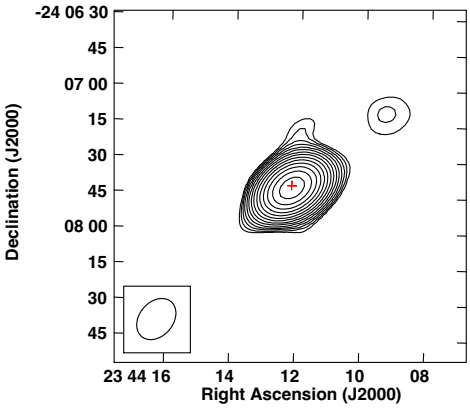

Figure A1. ASKAP continuum image of MRC 2341–244. The cross mark shows the continuum peak.

MRC 0042–248

The host of this radio source was classified as a galaxy by McCarthy et al. (1996), but an optical objective-prism spectrum published by Pocock et al. (1984) shows broad emission lines of C III] and Mg II at $z = 0.807$ – leading these authors to classify MRC 0042–248 as a quasar. Based on this, we have reclassified this object as a QSO rather than a galaxy.

MRC 0050–222

This source is not well-studied in the literature. It appears to be compact (angular size <0.5 arcsec) and core-dominated even at frequencies as low as 160 MHz, based on the scintillation index listed in Table 5. This implies a linear size smaller than about 3.5 kpc at the published redshift of $z = 0.654$, so we classify MRC 0050–222 as a compact steep-spectrum (CSS) source.

MRC 0106–233

Kapahi et al. (1998b) present a 4.8 GHz continuum image of this source, showing two lobes separated by about 3 arcsec. They note that the core emission in MRC 0106-233 is relatively weak (5 mJy at 8.4 GHz).

MRC 0118–272

The radio spectrum of this BL Lac object shows long-term variability (and a possible spectral peak) at frequencies above a few GHz. While the radio source is classified by Kapahi et al. (1998b) as unresolved at 5 GHz, IPS data (Table 5) suggest the presence of some extended emission at 162 MHz. The optical spectrum published by Falomo (1991) is largely featureless but shows a Mg II absorption doublet at $z = 0.557$. Since this may be an intervening line, Kapahi et al. (1998b) adopted a lower limit of $z > 0.557$ for the redshift of MRC 0118-227. Several later papers quote the redshift as $z = 0.557$ without acknowledging that this is only a lower limit.

MRC 0118–272 has been detected as an X-ray source by *Swift*/XRT (2SXPS J012031.6−270123; Evans et al. 2020), with an average rest-frame X-ray luminosity L(2–10 keV) of $>1.36 \times 10^{45}$ erg s^{-1} (this is a lower limit because we have only a lower limit to the redshift of this source).

MRC 0144–227

IPS measurements (Chhetri et al. 2018; see table 5) imply that this source is smaller than 1 arcsec in size at low radio frequencies. Based on its radio SED, we classify MRC 0144–227 as a CSS source.

MRC 0201–214

This object was identified as a peaked-spectrum radio source by Callingham et al. (2017).

MRC 0209–237

The 4.8 GHz continuum image published by Kapahi et al. (1998b) shows that this source is roughly 20 arcsec in angular extent, with a core and two prominent hotspots.

MRC 0209–237 was detected as an X-ray source by *ROSAT*/PSPC (2RXS J021129.4−232819; Boller et al. 2016). Converting to flux using the prescriptions of Dwelly et al. (2017), we estimate a rest-frame X-ray luminosity L(2–10 keV) of 1.0 ($\pm$0.3) $\times$ 10^{45} erg s^{-1}.

MRC 0223–245

Kapahi et al. (1998a) classify this as an unresolved source with an angular size <1 arcsec, and it is identified as a peaked-spectrum source by Callingham et al. (2017). The CASDA catalogue lists two continuum components for this source. This might indicate the presence of extended emission at lower frequencies, but the source also shows strong interplanetary scintillation suggesting that the weaker CASDA component could be an artefact.

MRC 0230–245

The 5 GHz image from Kapahi et al. (1998a) shows a pair of lobes separated by about 10 arcsec with no prominent radio core.

MRC 0233–290

No MWA IPS measurements are available for this object, but we tentatively classify it as a CSS source based on its compactness at 5 GHz (Kapahi et al. 1998a).

MRC 0418–288

The provenance for the redshift of z = 0.85 listed by Baker et al. (1999) is given as 'McCarthy 1994, private communication' and it appears that no published spectrum is available. We classify this as a CSS source based on its radio SED and compactness at 5 GHz (Kapahi et al. 1998a).

MRC 0531–237

This object was identified as a peaked-spectrum radio source by Callingham et al. (2017).

MRC 1002–216

Kapahi et al. (1998a) classify this as an unresolved source with an angular size <2 arcsec, and it is classified as a peaked-spectrum source by Callingham et al. (2017).

MRC 2156–245

Baker et al. (1999) show an optical spectrum of this quasar, noting that it has weak emission lines and that 'Mg II may be heavily absorbed'. As noted in the text, the optical redshift of z = 0.862 listed by Baker et al. (1999) is based on measurements of several emission lines and appears secure, so there is a significant velocity offset from the H I redshift of z = 0.8679. We classify this object as a CSS source.

MRC 2216–281

This object was identified as a peaked-spectrum radio source by Callingham et al. (2017).

MRC 2341–244

This source is relatively compact at 5 GHz (Kapahi et al. 1998a), but has a low NSI value of only 0.05 at 160 MHz – implying that extended emission contributes a significant fraction of the low-frequency flux density. The FLASH continuum image at 856 MHz (Fig. A1) shows two weaker sources within 1 arcmin of the MRC position that may account for the low NSI value. We have tentatively listed MRC 2341–244 among the CSS sources in Table 5, but caution that it may be an extended triple source rather than a genuine CSS object.

This paper has been typeset from a TEX/LATEX file prepared by the author.